Culture substrate stiffness impacts human myoblast contractility-dependent proliferation and nuclear envelope wrinkling

Jo Nguyen[1,2], Lu Wang[2,3], Wen Lei[4], Yechen Hu[5], Nitya Gulati[1], Carolina Chavez-Madero[1,2], Matthias Brandt[6], Timo Betz[7], Penney M. Gilbert[1,2,8*]

[1] Institute of Biomedical Engineering, University of Toronto, Toronto, ON, Canada

[2] Terrence Donnelly Centre for Cellular and Biomolecular Research, University of Toronto, Toronto, ON, Canada

[3] Department of Medical Biophysics, University of Toronto, Toronto, ON, Canada

[4] Faculty of Arts and Science, University of Toronto, Toronto, ON, Canada

[5] Department of Chemistry, University of Toronto, Toronto, ON, Canada

[6] Institute of Cell Biology, Center for Molecular Biology of Inflammation, University Münster, Münster, Germany

[7] Third Institute of Physics – Biophysics, Georg August University Göttingen, Göttingen, Germany

[8] Department of Cell and Systems Biology, University of Toronto, Toronto, ON, Canada

[*] Corresponding author

Email: penney.gilbert@utoronto.ca (PMG)

Abstract

The remarkable self-repair ability of skeletal muscle tissues is driven by muscle stem cells, whose activities are orchestrated by a variety of transient cues present in their microenvironment. Understanding how the cross-interactions of these biophysical and biochemical microenvironmental cues influences muscle stem cells and their progeny is crucial in strategizing remedies for pathological dysregulation of these cues in aging and disease. In this study, we investigated the cell-level influences of extracellular matrix ligands in the context of mechanically tuned culture substrates on primary human myoblast contractility and proliferation within 16 hours of plating. We found that fibronectin led to stronger stiffness-dependent responses in myoblasts compared to laminin and collagen as revealed by cell spreading area, focal adhesion morphology, traction stresses, and proliferation. While we did not observe stiffness-dependent changes in cell fate signatures at this early time-point, an analysis of the stiffness-sensitive myoblast proteome uncovered an enrichment for differentiation associated signatures on 17 kPa culture substrates, in addition to distinct profiles with relation to metabolism, cytoskeletal regulation, ECM interactions, and nuclear component enrichment. Interestingly, we found that softer substrates increased the incidence of myoblasts with a wrinkled nucleus, and that the extent of wrinkling could predict Ki67 expression. While nuclear wrinkling and Ki67 expression could be controlled by pharmacological manipulation of cellular contractility, cellular traction stresses did not correlate with nuclear envelope wrinkling level. These results provide new insights into the regulation of human myoblast stiffness-dependent contractility response by ECM ligands and also highlight a link between myoblast contractility and proliferation.

Introduction

The human skeletal muscle system sustains body mobility for many years owing to its self-repair capacity, powered by muscle stem cells (MuSCs). These MuSCs are scattered throughout muscle tissues in between muscle fibers and exist mostly in a quiescence state during homeostasis. In the event of tissue damage, MuSCs become activated, begin to proliferate, and either fuse into muscle fibers or self-renew. These processes are carefully regulated by biophysical and biochemical cues at the MuSCs residence over the tissue repair period[1,2]. MuSCs reside in a niche that is structurally polarized with the basal lamina on one side and the muscle fiber sarcolemma on the other. The basal lamina is a sheet of extracellular matrix (ECM) composed of laminins, collagens, fibronectin, and proteoglycans. During tissue repair, the ECM surrounding MuSCs can be both produced and degraded by many cell types including MuSCs themselves, causing fluctuations in its composition and physical properties like stiffness[2]. Stiffening of bulk muscle tissue and single myofibers occur upon damage[3–5], aging[4,6–9], exercise[10], and disease[11–14], while engineered niche stiffness has been shown to control myogenic cell activation[15], proliferation[4,5,16–18], differentiation[4,5,13,16,17,19], self-renewal[20], and division symmetry[21]. However, less explored is the role of specific ECM ligands in regulating stiffness-sensing in myogenic cells. Since irregular ECM remodeling is often involved in skeletal muscle aging and disease pathology, it is necessary to extend our understanding of the synergy between the physical and compositional changes in the ECM in controlling myogenic cell behavior.

MuSC adhesion to the ECM is mediated by transmembrane integrin receptors, with the most well-known being integrin α7, who together with the β1 subunit form binding receptors to niche laminin. MuSCs can also express integrins α3[22] and α6[23,24] while MuSCs progenitors in vitro express more integrin subtypes[25]. Integrin subtypes are specific to the presented ECM ligands, therefore any compositional changes in the ECM immediate to the MuSCs microenvironment hypothetically

would shift the profile of integrin subtypes recruited to the MuSCs membrane. For instance, laminin-α1 deposition has been reported to couple with the appearance of integrin α6 during MuSCs activation[24]. Since integrin subtypes can have differential binding mechanics with the ECM and thus tension-transmitting properties[26], ECM compositional dynamic not only could alter niche stiffness but potentially also how MuSCs "feel" that change. This hypothesis is challenging to test in the native MuSC niche, limited by the ability to manipulate physical niche factors without introducing chemicals disturbing the biochemical homeostasis. In vitro, murine MuSCs commitment to differentiation was reported to be sensitive to substrate stiffness on RGD-presenting hydrogels but not on laminin-presenting hydrogels[17]. MuSCs proliferation and migration have also been shown to be controlled by both ECM ligands and substrate stiffness by an unknown mechanism[17,27,28]. Deconstructing the interplay between ECM ligands and substrate stiffness converges at two questions: how ECM ligand identity changes the way myogenic cells sense substrate stiffness, and how substrate stiffness change ECM ligands signaling. In the current work, we contribute to the former question by characterizing the effects of ECM ligands on early adhesive and contractile response of myoblast to substrate stiffness, and then further emphasized the relationship between myoblast contractility and proliferation by reporting a correlation between nuclear envelope wrinkling level and Ki67 expression.

Materials and Methods

Fabrication of polyacrylamide (PAA) hydrogels

PAA hydrogels were fabricated according to the protocol described by Tse and Engler [29] with some modifications: hydrogels were cast on 35 mm glass bottom dishes (Matusunami Glass; D35-14-1-U) instead of coverslips, and deposition of NAOH was followed by immediate aspiration instead of heated evaporation. Hydrogels were then tethered with either fibronectin (Fibronectin bovine plasma, Sigma F1141), collagen (Collagen I, Rat Tail, Gibco A1048301), or laminin (Roche

93 11243217001) at a 100 mg/ml concentration according to Engler et. al. protocol. Expected
94 Young's moduli of the hydrogel formulations used in this study were extrapolated from the Engler
95 et. al. protocol (i.e., 1.10±0.34, 2.55±0.17, 4.47±1.19, 8.44±0.82, and 16.70) and were then
96 rounded to the nearest whole number: 1, 3, 5, 8, and 17 kPa, respectively, for simplicity.

97 For traction force microscopy, PAA hydrogels were fabricated following the same protocol above
98 with the addition of embedding 100 μm fluorescent beads at a 1:200 dilution.

99

100 **Primary human myoblast preparation and expansion**

101 Primary human myoblast cell lines were derived from human skeletal muscle biopsies. Four
102 primary human myoblast cell lines were used in this study: STEM21, STEM38, STEM86, and
103 UCAL38. For the STEM lines, the collection and use of the human skeletal tissues was reviewed
104 and approved by the Providence St. Joseph's and St. Michael's Healthcare Research Ethics
105 Board (REB# 13-370) and the University of Toronto Office of Research Ethics reviewed the
106 approved study and further assigned administrative approval (Protocol# 30754). For the UCAL38
107 cell line, the collection and use of the human skeletal tissues were reviewed and approved by the
108 University of Calgary Research Ethics Board (REB# 15-0005) and the University of Toronto Office
109 of Research Ethics reviewed the approved study and further assigned administrative approval
110 (Protocol# 34888). All procedures in this study were performed in accordance with the guidelines
111 and regulations of the respective Research Ethics Boards. Informed consent was obtained from
112 all donors. Table 1 summarizes muscle donors' information for each line.

113

114 **Table 1. Skeletal muscle biopsy donor information**

Cell line	Donor age	Donor sex	Muscle tissue source
STEM21	64	F	Multifidus muscle of patients undergoing lumbar spine surgery
STEM38	68	M	

STEM86	60	M	
UCAL38	64	M	Gracilis muscle from cadaveric donor within 4 hours of death

115

116 The establishment of primary human myoblast cell lines was described in previous reports[30,31].
117 To summarize, human skeletal muscle biopsies were minced and incubated with collagenase
118 (Sigma, 630 U/mL) and dispase (Roche, 0.03 U/mL) in Dulbecco's Modified Eagle's medium
119 (DMEM; Gibco) to digest the ECM and basal lamina. The resulting cell slurry was then passed
120 through a 20G needle multiple times to obtain a single-cell suspension, followed by incubation
121 with red blood cell lysis buffer (Table 2). The resulting non-purified cells were plated on collagen-
122 coated tissue culture dishes for one passage in myoblast growth medium (Table 2) and then were
123 immunostained and sorted using fluorescence-activated cell sorting (FACS), to purify the CD56+
124 myogenic progenitor population.

125 Myoblasts were expanded on collagen-coated tissue culture plastic plates before being collected
126 at passage 7-8 for experiments using the following method: adherent cells were first washed with
127 pre-warmed PBS, then incubated in 0.05 % trypsin-EDTA (Thermo Fisher Scientific, 25200072)
128 at 37 °C until all cells detached (about 5 minutes). After neutralizing trypsin-EDTA with growth
129 medium, the cell solution was centrifuged in 15 ml conical tubes at 300 G for 8 minutes, then
130 resuspended in 1 ml fresh growth medium. After cell-counting using a hemocytometer, 20,000
131 cells were seeded per hydrogel (diameter=12mm) for morphology, focal adhesion analysis, and
132 traction force microscopy experiments, while 25,000 cells were seeded per hydrogel for all other
133 experiments.

134

135 **Table 2. Cell culture media and solutions**

Media and solutions	Composition
RBS lysis buffer	ddH2O, 15.5 mM NH4Cl (Sigma-Aldrich, A9434), 1 mM KHCO3 (Sigma-Aldrich, 237205), 10 μM EDTA
Growth media	Ham's F-10 Nutrient Mixture (Wisent Bioproducts, 318-050-CL), 20% FBS (Gibco, 10437028), 5 ng/ml fibroblast growth factor-2 (ImmunoTools, 11343625), and 1% penicillin-streptomycin

136

137 **ML7 and LPA treatment**

138 Prior to NE wrinkling analysis, cells were treated with 25 μM ML7 for 1 hour before fixing, or with
139 50 μM LPA for 2 hours post-seeding, followed by a wash with media before incubating cells in
140 fresh growth media until the fixation time-point. Prior to Ki67 analysis, treatment with 10 μM ML7
141 or LPA was conducted overnight. In all of these conditions, the cells were fixed at 45 hours post-
142 seeding.

143

144 **Immunostaining**

145 Fixation was done by replacing half the volume of media in the culture dish with 4 %
146 paraformaldehyde (Electron Microscopy Sciences; 15714) in phosphate buffered saline (PBS)
147 followed by a 15-minute incubation. After three 5-minute PBS washes, cells were permeabilized
148 in 0.1 % Triton-X100 (BioShop, TRX777.500)/PBS for 15 minutes. Cells were then blocked in 10
149 % goat serum in PBS for 1 hour. Immediately after blocking, primary antibodies diluted in 1 %
150 goat serum were added and left overnight at 4 °C. The following day, after three 5-minute washes
151 in 0.025 % Tween-20 (BioShop, TWN510.500)/PBS, cells were incubated in secondary antibodies

152 and Hoechst counterstain diluted in 1 % goat serum for 1 hour. For F-actin visualization, Phalloidin
153 was also added at this step. Antibodies information and dilution are reported in Table 3. Before
154 imaging, cells were washed for 5 minutes in 0.0025 % Tween-20/PBS, then a final wash on a
155 gentle shaker for 30 minutes. All steps were done at room temperature unless specified otherwise.
156 For Pax7/MyoD experiments, after the final wash, PBS was removed then a coverslip was placed
157 on top of the cells, so that imaging was done through the top coverslip with the plate upside-down
158 in case PAA hydrogels with different stiffness alter the perceived fluorescence intensity of the
159 samples, even though this has not been reported as a concern in major PAA protocols[29,32]. In
160 other experiments where fluorescence intensity was not critical, imaging was done through the
161 bottom coverslip of the glass-bottom plate.
162
163 **Table 3. Antibody information**

Antibody	Host species	Dilution ratio	Manufacturer, catalog number
Hoechst 33342	-	1:1000	Thermo Fisher Scientific, H3570
Fluorescein Phalloidin	-	1:400	Molecular Probes, F432
anti-Paxillin, clone 5H11	mouse IgG1	1:200	Millipore Sigma, 05-417
anti-Pax7	mouse IgG1	1:1	In-house supernatant from hydridoma cell line (DHSB)
anti-MyoD1	mouse IgG2b	1:300	Santa Cruz Biotechnology, sc-377460

anti-Ki67	rabbit	1:300	Abcam, ab16667
anti-Lamin A/C	mouse IgG1	1:300	Santa Cruz Biotechnology, sc-376248
anti-Lamin A/C (H-110)	rabbit	1:300	Santa Cruz Biotechnology, sc-20681
Alexafluor™ 488 Anti-mouse IgG (H+L)	goat	1:300	Invitrogen, A11001
Alexafluor™ 647 Anti-mouse IgG1	goat	1:300	Invitrogen, A21240
Alexafluor™ 546 Anti-mouse IgG (H+L)	goat	1:300	Invitrogen, A11003
Alexafluor™ 546 Anti-mouse IgG2b	goat	1:300	Invitrogen, A21141
Alexa Fluor® 647 Mouse Anti-Human CD56 (NCAM-1)	mouse IgG1	1:20	BD Pharmingen, 557711

164

165 **Traction force analysis**

166 After 16 hours of culture on PAA hydrogels with embedded fluorescent beads (ThermoFisher
167 Scientific, F8800), the cells were stained for CellTracker Deep Red dye (ThermoFisher Scientific,
168 C34565) according to manufacturer's protocol. Imaging was done in FluoroBrite DMEM
169 (ThermoFisher Scientific, A1896701), 20 % FBS (Gibco, 10437028), and 1 % penicillin-
170 streptomycin solution medium. Images of beads and cells were taken before and after the addition

171 of 10 % sodium dodecyl sulphate (SDS). Traction stress maps were obtained using ImageJ
172 macros developed in prior published work [33,34]. Using MATLAB, cell masks were obtained by
173 expanding the original CellTracker binarized image by 70 pixels in all directions. Only traction
174 stress values inside the cell masks were considered.
175
176 **EdU assay**
177 After 16 hours of culture on hydrogel substrates, cells were pulsed with EdU at a concentration of
178 1 μM for 12 hours. Cells were fixed in 4 % PFA for 15 minutes and incubated in blocking solution
179 containing 10 % goat serum and 0.3 % Triton X-100 (BioShop, TRX777) diluted in PBS for 45
180 minutes at room temperature. EdU immunolabeling was done using the Invitrogen Click-iT EdU
181 kit according to the manufacturer's protocol (Invitrogen™, C10339) and then cells were
182 counterstained with Hoechst 33342.
183
184 **Viability assay**
185 After 16 hours of culture on hydrogel substrates, cells were washed with PBS, then incubated
186 with 1 μM calcein-AM (ThermoFisher Scientific, L3224), 1 μM propidium iodide (Sigma, P4864)
187 or ethidium homodimer-1 (ThermoFisher Scientific, L3224), and 1:1000 Hoechst in PBS for 20
188 minutes at room temperature. After removing the staining solution, cells were washed with PBS
189 and imaged immediately.
190
191 **Microscopy and image analysis**
192 Except for the EdU analysis, all microscopy was done with a Zeiss Axio Observer 7 microscope
193 equipped with LSM 800 scan head. A Plan-APO 40x/NA 1.40 Oil DIC objective was used for all
194 single cell analyses (i.e. paxillin, lamin A/C, traction force microscopy, and phalloidin
195 representative images), and a Plan-Apo 10x/NA 0.45 objective was used for cell spreading area
196 and the Ki67 imaging. EdU staining images were taken using an Olympus IX83 microscope

197 equipped with a DP80 dual CCD camera and either a LUCPLFLN PH 20x/ NA 0.46 or UPLFLN
198 2PH 10x/ NA 0.3 objective.
199 All image analysis was performed with ImageJ. FA alignment by goodness of fit (GoF) to a
200 Gaussian curve was obtained by running the Directionality ImageJ plug-in (written by Jean-Yves
201 Tinevez; https://imagej.net/plugins/directionality) on a random region of interest (ROI) close to the
202 cell periphery on the maximum projection of paxillin z-stacks. The analysis performed was based
203 on Fourier spectrum analysis. The percentage of total cells labeled by EdU was quantified by
204 dividing the number of segmented objects in the EdU channel by the number of segmented
205 objects in Hoechst channel. Nuclear wrinkling index was quantified using the ImageJ macro
206 developed by Cosgrove et. al [35] with some adjustments to allow semi-batch processing of our
207 datasets. The adapted macro used can be found in our public Github repository
208 (https://github.com/gilbertlabcode/Nguyen_PLOS_One2023). Ki67, Pax7, and MyoD
209 fluorescence intensities in each cell were quantified by measuring the integrated density inside
210 each nucleus. Binary binning (+/-) of Ki67, Pax7, and MyoD was done by identifying an intensity
211 threshold below which cells appear "negative" by reference to the secondary antibody controls.
212

213 **Lentiviral production**

214 Lentivirus particles were produced by calcium phosphate transfection, as reported previously[36].
215 Briefly, 35,000/cm^2 HEK 293T cells were seeded in a 10-cm culture plate and co-transfected 2
216 days later at 80 % confluency with second generation lentivirus system. Culture media (DMEM
217 supplemented with 10 % FBS) was refreshed prior to transfection, followed by addition of the
218 plasmid cocktail containing 4 µg of pMD2.G (a gift from Didier Trono; Addgene plasmid # 12259;
219 http://n2t.net/addgene:12259; RRID:Addgene_12259), 10 µg of psPAX2 (a gift from Didier Trono;
220 Addgene plasmid # 12260; http://n2t.net/addgene:12260; RRID:Addgene_12260) and 15 µg of
221 pLVX-EF1a-GFP-LaminA-IRES-Hygromycin [37] (a gift from David Andrews; Addgene plasmid #
222 134867; http://n2t.net/addgene:134867; RRID:Addgene_134867) for 12 hours. Culture media

223 was replaced to OptiMEM (Thermofisher, 31985062) 20mM HEPES (Sigma-Aldrich, 51558-
224 50ML), and the supernatant containing viral particles was collected at 24 and 48 hours after
225 transfection, passed through a 0.45 µm filter, and then concentrated using a 50 mL 100 000
226 MWCO spin column (Cytiva Life Sciences).
227
228 **Lentiviral transduction**
229 Primary human myoblasts were plated in a collagen-coated 6-well plate in growth media and
230 transduced when the cells were at about 50% confluency (i.e. ~ 24 hours after plating). 150-500
231 µL of viral supernatant containing 6 µg/mL polybrene (EMD Millipore, TR-1003-G) and was added
232 dropwise to the cells in fresh growth media and then incubated for 12 hours. The virus containing
233 media was aspirated and the cells were returned to regular growth media for 48 hours. The cells
234 were then trypsinized and seeded onto 17 kPa hydrogel substrates for 16 hours until traction force
235 microscopy experiment.
236
237 **Proteomics**
238 *Reagents*
239 Trypsin from bovine pancreas (Promega Biotec, V5113), lysine-C (New England BioLabs,
240 P8109S), protease and phosphatase inhibitor cocktail (ThermoFisher Scientific, 78442), formic
241 acid (FA, Sigma–Aldrich, F0507-100ML), tris(2-carboxyethyl) phosphine (TCEP, Sigma–Aldrich ,
242 C4706-2G), iodoacetamide (IAA, Sigma–Aldrich, I1149-5G), acetonitrile (≥ 99.9 %, CAN, Fisher
243 Chemicals, A9551), and water (Fisher Chemicals, W6-4).
244
245 *Preparation and digestion of protein extracts from myoblasts*
246 Myoblasts cultured on hydrogel substrates for 45 hours were collected by incubation with trypLE™
247 (ThermoFisher Scientific, 12604013). Cell numbers were determined by hemocytometer
248 counting. For each stiffness condition, a total number of 100,000 cells were washed three times

249 with cold PBS and resuspended in 20 µl lysis buffer (50 mM PBS, 1 % (v/v) protease inhibitor
250 cocktail). After three continuous freezing and defrost cycles, insoluble portions were separated
251 from the soluble portions by centrifugation at 16,000 × g for 20 minutes at 4 °C. Samples were
252 reduced in 10 mM TCEP (final concentration) at 70 °C for 30 minutes, alkylated with 20 mM IAA
253 (final concentration) in the dark at room temperature for 30 minutes, followed by incubation with
254 lysine-C (1:60) at 37 °C for 1.5 hr. Trypsin (1: 25) was then added and incubated at 37 °C for 16
255 hr. Finally, digests were quenched by the addition of 1 µL of concentrated formic acid.
256
257 *NanoRPLC-ESI-MS/MS methods*
258 Nanoflow reversed-phase liquid chromatography (NanoRPLC) was performed on an EASY-nLC
259 1200 ultra-high-pressure system coupled to a Q-Exactive HF-X mass spectrometer equipped with
260 a nano-electrospray ion source (Thermo Fisher Scientific). The obtained peptides were
261 automatically loaded onto a C18 trap column (100 µm i.d. × 5 cm) and separated by a C18
262 capillary column (100 µm i.d. × 15 cm). The trap column and the analytical column were both
263 packed in-house with 1.9 µm, 120 Å ReproSil-Pur C18 reversed phase particles (Dr. Maisch
264 GmbH). Two mobile phases (A: 0.1 % (v/v) FA and B: 80/20/0.1% ACN/water/formic acid (v/v/v)
265 were used to generate a 130 minutes gradient with the flow rate of 300 nL/minute (kept at 3 % B
266 for 5 minutes, 90 minutes from 3 % to 30 % B, 20 minutes from 30 % to 45 % B, 1 minutes from
267 45 % to 95 % B and 14 minutes to kept at 95 % B). MS was operated in full scan (120,000 FWHM,
268 400-1100 m/z) and data-independent acquisition (DIA) modes at positive ion mode. A 25.0 m/z
269 isolation window was set for MS/MS scan (60,000 FWHM) with stepped HCD collision energy of
270 25.5 %, 27 % and 30 %. The maximum IT for both MS and MS/MS was 254 ms. The electro-
271 spray voltage was 2.0 kV, and the heated capillary temperature was 275 °C. All the mass spectra
272 were recorded with Xcalibur software (version 4.1, Thermo Fisher Scientific).
273
274 *Database search*

275 DIA-NN 1.8 were applied for database searching against the Uniprot_Homo Sapiens database
276 (updated on 11/11/2021, 78120 entries) and the predicted spectrum library. The predicted
277 spectrum library was generated by DIA-NN 1.8 using the same database. The parameters of
278 database searching include up to one missed cleavage allowed for full tryptic digestion, precursor
279 ion mass tolerance and product ion mass tolerance were set 10 and 20 ppm, respectively,
280 carbamidomethylation (C) as a fixed modification, and oxidation(M), acetyl (protein N-term) as
281 variable modifications. Match between runs (MBR) was activated. Peptide spectral matches
282 (PSM) were validated based on q-value at a 1 % false discovery rate (FDR).
283
284 *Data processing*
285 Overrepresentation tests were done with PANTHER database version 17.0 released on 2022-02-
286 22 using Fisher's exact test with false discovery rate correction. For PANTHER pathways
287 annotation, the input was a list of differentially regulated proteins in both directions. For GO
288 cellular component annotation, the inputs were upregulated proteins in either soft or stiff
289 conditions.
290
291 **Data normalization**
292 Cell spreading area: Cell area data had a log-normal distribution (S1 A-B Fig). To meet the
293 normality assumption underlying the ANOVA test to compare the means between substrate
294 conditions, analysis was done based on the natural log of cell area (ln(Area)). Additionally, our
295 experiments were repeated on primary human myoblasts lines from independent donors. To
296 minimize cell line variance that may mask substrate effects, we normalized the mean ln(Area)
297 values to that of the values obtained on the 9 kPa condition for each cell line: normalized ln(Area)
298 = $\ln(\text{Area})/\ln(\text{Area})_{8kPa}$. Pre-normalized data is reported in S1 C-E Fig.
299 EdU assay: aside from reporting the unadjusted data, we scaled each cell line by the maximum
300 % total EdU+ value (scaled $x = x/x_{max}$) before linear regression fitting. Normalization by scaling

allowed us to focus on comparing the stiffness-dependent trends and minimized cell line variance in the exact values of % total EdU+ cells.

Statistical analysis

All statistical analysis was conducted using GraphPad Prism 6.0 software. To compare two conditions in experiments with one independent variable, comparisons were done with t-tests. To compare more than two conditions in experiments with one independent variable, a one-way ANOVA test preceded Holm-Šídák multiple comparison tests. For experiments with two independent variables, two-way ANOVA preceded Holm-Šídák multiple comparison tests. For all tests, α=0.05. p-values used to discuss comparisons between conditions are reported on top of graphs.

Table 4. Experimental replicate breakdown and statistical analysis

Figure	Cell number n and biological replicates N	Sample size n used for statistical analysis and error bars	Statistical analysis
1B	FN 1 kPa: n=515 FN 3 kPa: n=395 FN 5 kPa: n=548 FN 8 kPa: n=594 FN 17 kPa: n=601 LAM 1 kPa: n=567 LAM 3 kPa: n=471 LAM 5 kPa: n=414 LAM 8 kPa: n=455	n=3 from each condition	two-way ANOVA followed by Tukey's multiple comparison tests

	LAM 17 kPa: n=445 COL 1 kPa: n=920 COL 3 kPa: n=835 COL 5 kPa: n=884 COL 8 kPa: n=678 COL 17 kPa: n=899 from N=3.		
2C	FN 1 kPa: 32 FN 3 kPa: 28 FN 17 kPa: 26 LAM 1 kPa: 30 LAM 3 kPa: 30 LAM 17 kPa: 30 COL 1 kPa: 27 COL 3 kPa: 28 COL 17 kPa: 29 from N=3.	n=3 from each condition	two-way ANOVA followed by Holm-Šídák multiple comparisons tests
3B, 3C	FN 3 kPa: 22 FN 17 kPa: 20 LAM 3 kPa: 19 LAM 17 kPa: 21 COL 3 kPa: 24 COL 17 kPa: 22 from N=3.	n=3 from each condition	two-way ANOVA followed by a Holm-Šídák multiple comparison test

4B	FN 1 kPa: 691 FN 3 kPa: 923 FN 17 kPa: 655 LAM 1 kPa: 751 LAM 3 kPa: 854 LAM 17 kPa: 462 COL 1 kPa: 698 COL 3 kPa: 828 COL 17 kPa: 715 from N=3.	n=3 from each condition	two-way ANOVA followed by a Holm-Šídák multiple comparison test
4C	FN 1 kPa: 691 FN 3 kPa: 923 FN 17 kPa: 655 LAM 1 kPa: 751 LAM 3 kPa: 854 LAM 17 kPa: 462 COL 1 kPa: 698 COL 3 kPa: 828 COL 17 kPa: 715 from N=3.	n=3 from each condition	Linear regression
6B	Soft: 149 Stiff: 121 from N=3.	n=5 from each condition	one-way ANOVA followed by a Holm-Šídák multiple comparison test
6C	Soft: 105	N/A	No statistical analysis

	Stiff: 75 from N=3.		
6D	Soft: 105 Stiff: 75 from N=3.	n=3 from each condition	paired one-tail t-test
7B	Soft+DMSO: n=106 Stiff+DMSO: n=74 Stiff+ML7: n=78 from N=3.	n=3 from each condition	one-way ANOVA followed by a Holm-Šídák multiple comparison test
7C	Soft+DMSO: n=60 Stiff+DMSO: n=72 Soft+LPA: n=63 from N=3.	n=3 from each condition	one-way ANOVA followed by a Holm-Šídák multiple comparison test
7D	Soft+DMSO: n=1060 Stiff+DMSO: n=726 Stiff+ML7: n=657 Soft+LPA: n=688 from N=3.	n=3 from each condition	one-way ANOVA followed by a Holm-Šídák multiple comparison test
S3 Fig	Soft: 435 Stiff: 469 from N=3.	n=3 from each condition	

Representative image preparation

Figure 1: Cropped images were placed on a black background separated by white lines. Images were max projection of z-stacks.

318 Figure 2: Raw paxillin staining images were processed according to a published process [38] up
319 to the Log3D filtering step to create representative images. These images were then processed
320 with the Log3D plug-in, binarized, and cropped to create the insets.

321 Figure 3: Filtered stress maps were created following the process written in the “Traction force
322 analysis” section above.

323 Figure 4: The brightness and contrast of raw EdU and Hoechst images were equally adjusted in
324 all conditions.

325 Figure 5: Individual nuclei were cropped from raw Lamin A/C images. The brightness and contrast
326 of Lamin A/C were equally adjusted for all nuclei.

327 Figure 6: Images from the first three conditions (soft+DMSO, stiff+DMSO, stiff+ML7) were
328 collected from the same experiment so their brightness and contrast were adjusted equally. The
329 images for the soft+LPA condition were collected from a separate experiment, and thus, the
330 brightness and contrast were adjusted to most closely match that of the other conditions. Note
331 that fluorescence intensity was not considered in the analysis of these results.

332

333 ## Results

334 **Accentuated myoblast stiffness sensitivity observed on fibronectin-tethered substrates**

335 We first explored the influence of ECM ligand tethering on human primary myoblast responses
336 associated with stiffness-sensing that included cell spreading area, focal adhesion assembly, and
337 traction stress. We followed a well-established poly-acrylamide (PA) hydrogel fabrication protocol
338 to create cell culture substrates with tuned stiffness that we then tethered with ECM ligands found
339 within the native muscle stem and progenitor cell microenvironment: fibronectin (FN), laminin
340 (LAM), or collagen-1 (COL)[29]. We selected PA gel stiffnesses of 1, 3, 5, 8, and 17 kPa to mimic
341 the reported range of the Young's modulus of skeletal muscle and single muscle fibers, which

342 were reported to be approximately 0.2-18 kPa, spanning healthy, damaged, and aged states
343 [4,13,20,21,39,40].

344 16 hours after plating on FN substrates, human primary myoblast cell spreading was minimal on
345 1 kPa culture substrates, noticeably increased at 3kPa, then plateaued from 3 to 17 kPa (Fig 1).
346 Cell spreading on LAM substrates presented a similar relationship with culture substrate stiffness,
347 although a slight decrease in spreading at 17 kPa was observed. By contrast, cells on COL
348 substrates attained equally large spreading area independent of culture substrate stiffness within
349 the tested stiffness range, except for a decrease at 17 kPa (Fig 1A-B). As we only included well
350 isolated mononucleated cells in our analysis, the decrease in spreading area at 17 kPa may have
351 been an analysis artifact due to the greater likelihood of larger cells making physical contact with
352 neighboring cells.

353 Next, we visualized adhesion structures with paxillin immunostaining and noted that the paxillin
354 structures detected had a broad range of sizes (Fig 2A). On the 1 kPa substrates tethered with
355 FN and LAM, wherein the myoblasts had minimal spreading, we observed long paxillin+ structures
356 outlining the nucleus and/or the peripheral edges of the cells. The appearance of cells with these
357 features was rare on the higher substrate stiffnesses and were also rare on the COL tethered
358 substrates more generally. Adhesion structure morphologies varied along three scales: within a
359 single cell, across different cells cultured on the same substrates, and between the biological
360 replicate cell lines. These variabilities made it challenging to attribute substrate effects to adhesion
361 size and shape, which, by themselves, are insufficient to infer focal adhesion function and maturity
362 [41]. For this reason, we instead chose to quantify local adhesion structure alignment. Since cells
363 exert traction forces through adhesion structures where stress fibers terminate, the alignment of
364 adhesion structures is indicative of the alignment of stress fibers and provides a speculative
365 imagery of the cell contractility state[42,43]. To measure the alignment of adhesion structures, we
366 used the “Directionality” ImageJ plugin, which generates a frequency distribution histogram of

367 structures over a range of direction angles (with 0° being the East direction and going
368 counterclockwise). The histogram was then fitted to a Gaussian curve. If the structures in the
369 region of interest align in a common direction, the histogram will have a peak and resemble a
370 Gaussian curve, thus having a high goodness of fit (GoF) (Fig 2B, top). Conversely, if a common
371 direction of alignment does not exist, the histogram will be flat and have a low GoF (Fig 2B,
372 bottom). The alignment of paxillin structures across substrate conditions showed trends like the
373 cell spreading area data (Fig 1). Specifically, on FN and LAM substrates, GoF was low at 1kPa,
374 increased at 3kPa and then remained relatively constant at 17kPa, although the increase on LAM
375 substrates was more subtle, and did not reach statistical significance in our study (Fig 2C). On
376 the COL substrates, adhesion structures reached equally high alignment regardless of substrate
377 stiffness (Fig 2C).

378 Although cell spreading area and adhesion alignment did not differ significantly between 3 and 17
379 kPa on FN substrates, upon conducting traction force microscopy studies, we observed a
380 significant increase in mean and max traction stress across these conditions. Similar trends were
381 seen on the LAM and COL substrates, though the magnitude of the effect was more subtle than
382 on the FN condition (Fig 3A-C).Traction data on 1 kPa substrates were excluded from this analysis
383 because we were unable to reliably derive cellular traction stress with our workflow because of
384 the extremely large hydrogel deformations. Likely due to large deformation caused on softer
385 hydrogels, even though lower stresses were recorded on 3 kPa substrates compared to 17 kPa,
386 strain energy was generally higher on 3 kPa than 17 kPa in all ECM conditions, but was only
387 statistically significant for COL (S3 Fig).

388 In summary, by evaluating the morphology, focal adhesion arrangement, and cellular traction
389 stress of primary human myoblasts cultured on 1, 3, and 17kPa PA hydrogels, we found that FN-
390 tethered hydrogel substrates encouraged more pronounced stiffness sensitivity when compared
391 against the LAM- and COL- tethered substrates, in terms of the above metrics.

392 **ECM ligands influence the linearity of proliferation correlation with substrate stiffness**

393 To probe whether ECM ligands also tune cellular functional response to substrate stiffness, we
394 evaluated myoblast proliferation using the 5-ethynyl-2'-deoxyuridine (EdU) assay. After cells were
395 cultured for 16 hours on hydrogel substrates, we added EdU in the culture media for 12 hours.
396 The percentage of EdU+ cells increased steadily from 1 to 17 kPa for myoblasts cultured on FN-
397 tethered substrates (Fig 4B). For LAM- and COL-tethered substrates, the percentage of EdU+
398 cells showed an insignificant, trended increase from 1 to 3 kPa and then remained constant from
399 3 to 17 kPa. We suspected that myoblast proliferation and substrate stiffness had a positive, linear
400 correlation on FN but not on LAM and COL substrates. To assess linearity, we scaled %EdU+
401 values to minimize cell line variance while maintaining the correlation slope (refer to Methods)
402 then performed linear regression fitting. On FN substrates, %EdU+ cells and substrate stiffness
403 were indeed linearly fitted with an r^2=0.7 while LAM and COL were poorly linear with r^2 values of
404 0.3 and 0.2 respectively. The correlation slope in FN condition was also significantly non-zero
405 with p=0.007 while p-values for LAM and COL were higher at 0.160 and 0.291 (Fig 4C). To
406 eliminate the possibility that non-proliferative cells were instead undergoing apoptosis, we
407 performed a live/dead assay, whose result indicated that all cells across all stiffnesses on FN-
408 tethered substrates were calcein-AM positive and propidium iodide negative (S2 Fig).

409

410 **Nuclear envelope (NE) wrinkling can predict Ki67 expression**

411 In conducting EdU analysis, we noticed qualitatively that there were more cell nuclei with odd
412 shapes on softer substrates, so we asked if NE morphology regulation could be upstream of
413 stiffness-dependent proliferation control. We followed through with a series of experiments
414 focusing on two conditions: soft (1kPa) and stiff (17kPa) FN substrates. Immunostaining for Lamin
415 A/C revealed a heterogeneity in NE shapes on both stiffnesses: some nuclei were taut and oval-
416 like, as generally expected for adherent cells, but some were severely wrinkled (Fig 5A). We
417 quantified NE wrinkling by measuring wrinkle index (WI) using an ImageJ macro developed by

418 Cosgrove et al. with minor modifications[35]. We found that taut nuclei with no or minor folding
419 have WI ≤ 20%, whereas wrinkled nuclei have WI > 20%. Noticeably, the percentages of wrinkled
420 nuclei, defined by WI > 20%, were two times higher on soft compared to stiff FN-tethered
421 substrates (around 40% and 19%, respectively).
422 We further plotted Ki67 intensity against the WI of each cell in each stiffness condition. Ki67
423 intensity levels were either negative, low positive (cells in active cell cycle but not S-phase), or
424 high positive (cells in S-phase)[44]. We observed that although a taut nucleus did not always have
425 high Ki67 intensity, a nucleus with high Ki67 intensity was always taut (WI ≤ 20%), at least in the
426 three cell lines studied (Fig 5C). Wrinkled nuclei were four times less likely than taut nuclei to be
427 Ki67+ at any intensity (Fig 5D).

428 In summary, there were higher incidences of wrinkled nuclei when myoblasts were cultured on
429 soft substrates, and myoblasts with wrinkled nuclei did not express high levels of Ki67.

430 **Pharmacological manipulation of contractility modulates NE wrinkling level and myoblast**
431 **proliferation**

432 Cellular contractile force is transmitted by actin retrograde flow from adhesion sites towards the
433 cell center, where the cytoskeleton is directly linked to the nucleus[45–47]. To investigate if low
434 contractility on soft substrates causes NE wrinkling in myoblasts, as has been observed in
435 mesenchymal stromal cells (MSCs)[35], we mirrored established methods to pharmacologically
436 inhibit and activate cellular contractility using a myosin light chain kinase inhibitor (ML7) and
437 lysophosphatidic acid (LPA), respectively. Consistent with MSCs studies, we found that ML7
438 treatment increased the percentage of wrinkled nuclei on stiff substrates, while LPA treatment
439 lowered the incidence of wrinkled nuclei on soft substrates, although the effect was not as
440 pronounced as ML7 (Fig 6A-C). Additionally, overnight treatments of ML7 decreased the
441 proportion of Ki67+ myoblasts present on stiff culture substrates, while LPA increased Ki67+
442 proportion on soft substrates (Fig 6D).

443 With these results, we hypothesized that cellular traction stresses would be lower in cells with
444 wrinkled nuclei (WI > 20) compared to cells with taut nuclei (WI ≤ 20%). To test this hypothesis,
445 we conducted traction force microscopy on myoblasts cultured on 17 kPa FN substrates
446 expressing a live Lamin A reporter, the pLVX-EF1a-GFP-LaminA-IRES-Hygromycin plasmid [37].
447 Unexpectedly, traction stresses and strain energy values were similar between cells with taut and
448 wrinkled nuclei (Fig 6 E-G, S4 Fig). This suggests that the relationship between cellular
449 contractility and NE wrinkling is not straightforward. It is possible that cells with wrinkled nuclei on
450 1 kPa substrates had lower traction stresses than those on 17 kPa. But if low contractility was the
451 only cause of NE wrinkling, a negative correlation between contractility and WI would have been
452 observed among cells on the same substrate stiffness.

453 In summary, it appears that pharmacological manipulation of cellular contractility can alter NE
454 wrinkling, and the absence of NE wrinkling seems to be a prerequisite for high Ki67 expression in
455 myoblasts. However, low cellular contractility is likely not the only cause of NE wrinkling.

456 **Proteomic assessment of myoblast cellular processes and fate**

457 To gain a comprehensive understanding of cellular processes following the initial responses to
458 substrate stiffness, we profiled the proteomes of 100,000 cells cultured for 45 hours on either 1
459 or 17 kPa FN-tethered substrates, between which we saw the most distinct differences in cellular-
460 level responses. We will refer to these conditions as “soft” and “stiff” substrates in subsequent
461 discussions. 100,000 cells in each stiffness condition were split into three technical replicates. All
462 proteomic data and analysis are provided in the supporting information.

463 Over 3216 protein groups were detected across the three technical replicates, and only groups
464 with quantitative information in at least 2 out of the 3 replicates were considered. Myoblasts
465 cultured on soft and stiff substrates had distinguishable proteomic profiles (S5A Fig). Among
466 these filtered protein groups, 838 were determined to be differentially expressed by a $p < 0.05$
467 cut-off (S5B Fig). Using the PANTHER database to analyze differentially expressed proteins, we

468 identified 5 enriched pathways: pentose phosphate pathway, glycolysis, integrin signaling
469 pathway, cytoskeletal regulation by Rho GTPase, and Huntington disease (Fig 7A). The
470 enrichment of integrin signaling and cytoskeletal regulation by Rho GTPase are expected in the
471 context of adherent cell stiffness-sensing. Cancer cells cultured on soft environments have been
472 reported to have reduced metabolic activities which may play a role in decreasing proliferation
473 rate[48]. With the top two overrepresented pathways in our proteomic analysis being pentose
474 phosphate pathway and glycolysis, we further looked at the expression of components of these
475 metabolic pathways, and ATP synthases, for evidence of myoblasts potentially being
476 metabolically dormant on soft substrate. Many enzymes catalyzing chemical processes in
477 pentose phosphate pathway and glycolysis were detected to have been more abundant on soft
478 substrates, and ATP synthase subunits expressions had mixed correlation with substrate stiffness
479 (S6A-B Fig). Without measuring direct metabolic outputs such as ATP levels, whether there was
480 a metabolic halt on soft substrates remained a standing question, but our proteomic assessment
481 suggests that if there was a halt, it likely would not have been due to the lack of metabolic enzymes
482 or ATP synthase.

483 Myogenic proliferation and differentiation are regulated by a series of transcription factor activities.
484 In vitro, myoblast fate signatures are often profiled by assessing expression of the transcription
485 factors Pax7 and MyoD: Pax7+/MyoD- (stem-like or reserve-like cells), Pax7+/MyoD+
486 (proliferative cells), and Pax7-/MyoD+ (differentiating cells). We asked whether there was an
487 increase in the proportion of either reserve-like or differentiating cells that might have
488 corresponded to the larger portion of non-proliferative cells observed on soft culture substrates.
489 We found that the proportions of fate signatures were similar on both stiffnesses, with most cells
490 being Pax7+/MyoD+ (S7A-B Fig). Interestingly, the proteomics data reported an overall lower
491 MyoD expression for myoblasts cultured on soft substrates (Fig 7B), while desmin, a myogenic
492 commitment marker, was expressed at a higher level on stiff substrate (Fig 7B). Furthermore,

493 JUNB, which has been previously reported to suppress myogenin expression[49], was found to
494 express at a higher level on soft substrate (Fig 5 B). Our immunocytochemical analysis suggests
495 that there may not have been a major divergence in the Pax7/MyoD myogenic fate landscape
496 across the two substrate stiffness levels at the 45-hour time-point post-seeding in growth medium.
497 However, based upon the proteomics assessment a stiff substrate at 17 kPa would favor a more
498 differentiative phenotype while soft substrate would favor a more reserve-like phenotype. To
499 significantly cultivate these fate transitions, we expect that other factors like culture time and
500 medium composition would need to be redesigned.

501 We noticed higher expressions of ECM proteins like FN1, several COL alpha units, and LAMC1
502 in cells on soft substrate (Fig 7D), which could suggest that myoblasts were actively attempting
503 to modify their environment thus not being completely inactive on soft substrate.

504 We also performed gene ontology (GO) overrepresentation tests on proteins upregulated in either
505 soft or stiff condition. For these tests, we further filtered differentially expressed proteins by their
506 fold change (stiff/soft). Only proteins with fold change less than or equal to 0.9, or more than or
507 equal to 1.1 were considered. Among the top five enriched cellular components in either stiffness
508 were several nuclear components (Fig 7E). LMNA expression level was found to be higher on
509 stiff substrate. Since outside-in environmental signal transduction into cellular function converges
510 at the level of transcription, major changes happening in the nucleus could provide important
511 insights into how substrate stiffness is transduced into a proliferation response.

512

513 **Discussion**

514 In this work, we characterized the short time-point, ECM ligand-specific cellular responses of
515 primary human myoblasts cultured on mechanically tuned polyacrylamide-based hydrogels,
516 described the substrate stiffness-specific proteomes of human myoblasts, and reported that

517 nuclear envelope wrinkling can predict myoblast cell cycle state. Our study revealed that FN
518 ligand tethering led to more exacerbated substrate-stiffness-dependent morphological,
519 contractile, and proliferative responses in myoblasts compared to LAM and COL. We reported
520 that the myoblast proteome responds to stiffness by differentially regulating metabolic, Rho
521 cytoskeletal regulation and integrin signaling pathways, with interesting enrichment of nuclear
522 components. Lastly, heavily wrinkled nuclear envelope morphology can predict the absence of
523 Ki67 expression, which can be restored by LPA treatment.

524 The dependence of stiffness-sensing mechanics on ECM ligand is an understudied realm of
525 myogenic cell mechanosensing. ECM ligands bind to specific integrin receptors, which have
526 distinct molecular force transmission mechanics[26]. For example, the FN-integrin α5 bond
527 requires the tension-dependent conformational change of FN to expose a hidden energy site,
528 while COL can bind tension-independently to integrin α2, leading to substrate stiffness-dependent
529 FAK activation on FN-presenting substrates but not those presenting COL[50]. The effects of
530 ECM ligands on myogenic cell stiffness-sensing appear to vary depending on the species and
531 passage number of myogenic cells studied and the specific experimental parameters [17,27,28].
532 In our experiments, we observed that relative to LAM and COL, culturing myoblasts on FN-
533 tethered hydrogels led to more exacerbated stiffness-sensitivity in terms of cell spreading,
534 adhesion alignment, cellular traction, and proliferation. At longer culture time and higher stiffness
535 range, murine MuSCs proliferation have been shown to be stiffness-dependent on both LAM and
536 RGD-presenting hydrogels, while MyoG commitment was stiffness-dependent on RGD and not
537 LAM[17]. Confounding factors to PA hydrogel Young's modulus, such as porosity and ligand
538 tethering density could potentially add to result variability[51,52].

539 The idea that ECM composition could potentially alter myogenic cells mechano-sensitivity is
540 important in the context of in vivo niche ECM remodeling during regeneration, aging and disease.
541 MuSCs niche factors were reported to actively suppress activation pathways to maintain MuSCs

542 quiescence[53,54]. As for LAM, past studies have shown that laminin-2/4 deficiency leads to the
543 loss of integrin α7β1[55], which in turn could disrupt quiescence maintenance[56]. We can
544 therefore infer that the SC connection to LAM via integrin $\alpha 7\beta 1$ is important in preserving SC
545 quiescence, but the exact mechanisms are unknown. In vitro studies on myoblasts, in agreement
546 with other cell types, showed that LAM preferentially activates Rac and suppresses RhoA[57]. In
547 contrast with FN, LAM promotes motile cells with diffused stress fibers and poor vinculin-
548 containing adhesion assembly, characteristic of a high Rac/low RhoA phenotype[58]. These
549 observations are exciting in the context of the Rac-to-Rho switch occurring during MuSCs
550 activation[59]. Rho-regulated cytoskeletal remodeling is critical in cell tension sensing, including
551 matrix stiffness. It is therefore enticing to explore the possibility that LAM actively suppresses
552 MuSCs mechanosensing, while FN enrichment in the injured niche increases MuSCs sensitivity
553 to injury sensation and facilitates the quiescent to proliferative transition, and furthermore, how
554 age- and disease-related irregular ECM deposition impair MuSCs sensitivity to niche remodeling.

555 MuSCs are functionally heterogeneous[60], as are their downstream progenitors. Our results
556 suggested that relatively stiff substrates, tethered with FN, decrease myoblast cell cycle
557 heterogeneity, cultivating a primarily proliferative population. While we observed that soft
558 substrates tethered with FN increased the incidence of Ki67- myoblasts, we did not assess
559 whether the cell cycle itself was impeded. Regarding the split between Ki67+ and Ki67- myoblasts
560 on the same substrate stiffness, our data suggested that perhaps one of the differences between
561 these subpopulations is their contractility, since high Ki67 expression was only observed in the
562 absence of NE wrinkling, a state typically characterized by high cellular contractility[35]. To assess
563 the correlation between cell contractility and NE wrinkling level, we performed traction force
564 microscopy on cells expressing a live Lamin A reporter. To our surprise, cellular traction stress
565 and strain energy were independent of NE wrinkling index, despite pharmacological manipulation
566 of contractility resulting in expected NE wrinkling and Ki67 expression responses. There are a

few possible explanations. First, pharmacological manipulation experiments were done on two substrate elasticities while traction force microscopy on Lamin A-GFP expressing cells were conducted exclusively on 17 kPa substrates, so it is possible that cells with wrinkled nuclei on 1 kPa had lower traction stresses than cells with wrinkled nuclei on 17 kPa. Second, our proteomic analysis detected a decrease in Lamin A/C on soft substrate, which could potentially take part in increasing NE wrinkling[61,62]. Third, we did not assess nuclear-actin connectivity. If there is a disruption in tension propagation from the cytoskeleton to the nucleus, nuclear tension would be low regardless of cytoskeletal contractility. For example, severing the Linker of Nucleoskeleton and Cytoskeleton (LINC) complex has been shown to induce similar nuclear wrinkling phenotypes[35,63].

Whether and how exactly NE wrinkling could suppress proliferation are questions whose pursuit would require the manipulation of NE wrinkling without altering cellular signaling, which is a limitation of the pharmacological strategies that we and others use to manipulate contractility. LPA activates a range of signaling pathways including Ras and Rho/ROCK GTPases which are cell cycle regulators[64–66]. Alternatively, low nuclear tension reduces nucleocytoplasmic exchange of signaling molecules like YAP, cyclin B1, and MyoD by potentially deforming nuclear pore complexes[67–69]. Cosgrove et al. reported a correlation between NE wrinkling and YAP/TAZ nuclear localization in mesenchymal stem cells [35]. In our system, bulk proteomic profiling on soft and stiff substrates did not detect differential YAP target proteins between soft and stiff substrates, suggesting that a YAP/TAZ localization mechanism may not underlie our results.

In conclusion, our work emphasized the integrated control of substrate stiffness and ECM composition on myoblast contractility and proliferation, which are heterogeneous phenotypes intimately linked to the NE morphology. The impact of our work extends to biomaterial design applications and implicates fundamental regulation of human myogenic cell mechanosensing.

Acknowledgements

592 We would like to thank Dr. Qingzong Tseng for advice on the implementation of his TFM ImageJ
593 macros and Dr. Louise Moyle for thoughtful discussions. This work was funded by a Natural
594 Sciences and Engineering Research Council grant to P.M.G. (RGPIN-2019-07144), a Human
595 Frontiers Science Program (RGP0018/2017) to P.M.G. and T.B., a Deutsche
596 Forschungsgemeinschaft (DFG, BE 6270/2-1) to TB, a Connaught International Scholarship to
597 J.N., and a Canada Research Chair in Endogenous Repair to P.M.G. (#950-231201).
598

599 **Author contributions**

600 Conceptualization: J.N., P.M.G.; methodology: J.N., L.W., M.B.; investigation: J.N., L.W., W.L.,
601 Y.H., N.G., C.C.M.; validation and formal analysis: J.N., W.L., L.W., Y.H., N.G.; visualization:
602 J.N., writing-original draft and writing-review & editing: J.N., P.M.G.; supervision and funding
603 acquisition: T.B., P.M.G. All authors approved the final manuscript.
604

605 **Conflict of Interest**

606 The authors have no conflict of interests that might be perceived to influence the results or
607 discussion reported in this paper.
608

609 **Figure Legends**

610 **Fig 1. Cell spreading area characterization across substrate stiffness and ECM conditions.**
611 **A** Representative confocal images of phalloidin staining in primary human myoblasts cultured for
612 16 hours on 1, 3, 5, or 17 kPa polyacrylamide gels tethered with fibronectin (FN), laminin (LAM),
613 or collagen 1 (COL). Phalloidin-cyan, Hoechst-yellow. scale bar=50 μm **B** Graphs showing mean
614 cell spreading area across hydrogel stiffness, in FN, LAM, and COL conditions, in terms of fold
615 change with respect to the 8 kPa condition (dotted line at y=1). Each data point represents the
616 mean of one biological replicate. n=395-920 cells per condition across N=3 biological replicates.

617 Error bars report mean ± SD. Statistical comparisons were made by two-way ANOVA followed by
618 Tukey's multiple comparison tests.
619
620 **Fig 2. Adhesion alignment characterization across substrate stiffness and ECM conditions.**
621 **A** Representative confocal images of primary human myoblasts adhesion structures 16 hours
622 post-seeding on fibronectin (FN), laminin (LAM) or collagen 1 (COL) tethered polyacrylamide gels.
623 Paxillin-yellow, Hoechst-blue. Scale bar=20 μm. **B** Representative directionality histograms of a
624 paxillin staining ROI with goodness of fit to a Gaussian curve (GoF) = 0.24 (top) and an ROI with
625 GoF=0.84 (bottom). y-axis is the frequency of structures detected by the algorithm and x-axis is
626 the angle direction of those structures with respect to a horizontal line (°) **C** Bar graph showing
627 GoF as a metric of adhesion alignment. Each data point represents the mean of one biological
628 replicate. n=26-32 cells per condition across N=3 biological replicates. Error bars report mean ±
629 SD. Statistical comparisons were made by two-way ANOVA followed by Holm-Šídák multiple
630 comparisons tests.
631
632 **Fig 3. Cellular traction stress measurement across substrate stiffness and ECM**
633 **conditions. A** Representative traction stress maps of myoblasts 16 hours post-seeding on
634 fibronectin (FN), laminin (LAM) or collagen 1 (COL) tethered polyacrylamide gels. Scale bar=20
635 μm **B and C** Bar graphs showing mean and max traction stress, respectively, across substrate
636 stiffness and ECM conditions. n=19-24 cells per condition across N=3 biological replicates. Each
637 data point represents the mean of one biological replicate. Error bars report mean ± SD. Statistical
638 comparisons were made by two-way ANOVA followed by a Holm-Šídák multiple comparison test.
639
640 **Fig 4. Myoblast proliferation exhibits a more linear correlation with stiffness on fibronectin**
641 **(FN) substrates. A** Representative immunostaining images of EdU incorporation assay at 16hr

post-seeding on fibronectin (FN), laminin (LAM) or collagen 1 (COL) tethered polyacrylamide gels followed by a 12hr EdU pulse. EdU-yellow, Hoechst-cyan. Scale bar=100 μm. **B** Line graph showing the mean ± SD of % total EdU+ cells. Statistical comparisons were made by two-way ANOVA followed by Holm-Šídák multiple comparison test **C** Linear regression lines of the same data set in B. EdU percentages scaling was conducted by normalizing to the max value of each cell line in order to eliminate cell line variation (scaled $x = x/x_{max}$). Legend displays r^2 (goodness of fit) and p-value testing to determine whether the slope of the fitted line is significantly non-zero. Each data point represents the mean of one biological replicate. n=462-923 cells per condition across N=3 biological replicates.

Fig 5. Stiffness-dependent heterogeneity in nuclear envelope wrinkling predicts Ki67 status. A Representative confocal images of taut (wrinkle index (WI)≤20) and wrinkled (WI>20) nuclear envelopes. Lamin A/C-cyan. Scale bar=10 μm. **B** Bar graph showing the percentages of taut and wrinkled nuclei on soft and stiff substrates. Each data point represents the mean of one independent technical replicate. Error bars report mean ± SD. n=149-121 cells per condition across N=5 independent experiments on 3 different cell lines. Statistical comparison was made by one-way ANOVA followed by a Holm-Šídák multiple comparison test **C** xy plot with x=WI (%) and y=normalized Ki67 fluorescence intensity (arbitrary unit). Each data point represents one cell. n=180 cells total across N=3 biological replicates **D** Bar graph comparing the percentage of Ki67+ nuclei in taut and wrinkled nuclei populations. n=180 cells total across N=3 biological replicates. Statistical comparison was made by a paired one-tail t-test.

Fig 6. ML7 and LPA treatments alter myoblast nuclear envelope wrinkling and proliferation. A Representative confocal images of nuclear envelope wrinkling in myoblasts cultured on soft (1 kPa) fibronectin-tethered polyacrylamide substrates treated with either DMSO (soft+DMSO) or

667 LPA for 2hr (soft+LPA), and in myoblasts cultured on stiff (17 kPa) fibronectin-tethered substrate
668 treated with either DMSO (stiff+DMSO) or ML7 1hr before fixing (stiff+ML7). Lamin A/C-cyan.
669 Scale bar=10 μm. **B** Bar graph showing the percentages of wrinkled nuclei (WI>20) in
670 soft+DMSO, stiff+DMSO, and stiff+ML7 conditions. n=74-106 cells per condition across N=3
671 biological replicates. **C** Bar graph showing the percentages of wrinkled nuclei in the population of
672 myoblasts cultured in soft+DMSO, stiff+DMSO, and soft+LPA conditions. n=60-72 cells per
673 condition across N=3 biological replicates. **D** Bar graph showing the percentage of Ki67+
674 myoblasts when cells cultured on stiff and soft substrates were treated with, respectively, ML7
675 and LPA, both at 10 μM overnight, in comparison with DMSO controls. n=657-1060 cells across
676 N=3 biological replicates. For all graphs, each data point represents the mean of one biological
677 replicate. Error bars report mean ± SD. Statistical comparison was made by one-way ANOVA
678 followed by a Holm-Šídák multiple comparison test. **E** Representative traction stress maps of a
679 cell with a taut nucleus and a cell with a wrinkled nucleus. Scale bar = 10 μm. **F-G** Bar graph
680 showing the mean and max traction stress of cells with taut and wrinkled nuclei. n=7-9 cells in
681 each condition across two technical replicates of one Lamin A-GFP transduced cell line.

682 **Fig 7. Profiling myoblast proteomes on fibronectin-tethered soft (1 kPa) and stiff (17 kPa)**
683 **culture substrates at 45 hr post-seeding A** Overrepresented PANTHER pathways from the list
684 of differentially expressed proteins upon comparing human myoblasts cultured on soft and stiff
685 fibronectin-tethered polyacrylamide substrates **B** Differentially expressed myogenic-relevant
686 markers **C.** Differentially expressed major cell cycle regulators **D** Differentially expressed proteins
687 with direct ECM interactions **E** Table showing top five enriched cellular components from GO
688 cellular component annotation of proteins upregulated in soft and stiff substrate conditions.
689

690 **S1 Fig. Log-normal cell spreading area distribution A** Frequency distribution of raw,
691 unadjusted myoblast cell spreading areas on 1 kPa fibronectin-tethered polyacrylamide

692 substrates **B** Frequency distribution of the natural log of the same cell spreading area data as in
693 A. **C, D, E** Graphs showing the natural log of myoblast spreading area before normalizing to 9
694 kPa condition. Each data point represents the mean of one biological replicate. n=395-920 cells
695 per condition across N=3 biological replicates. Error bars report mean ± SD.
696

697 **S2 Fig. Viability analysis of myoblasts cultured on fibronectin-tethered polyacrylamide**
698 **substrates.** Representative images of human myoblasts cultured for 16 hours on 1, 3, or 17 kPa
699 fibronectin-tethered polyacrylamide substrates and stained for Hoechst (yellow), propidium iodide
700 (PI; magenta) and Calcein (green). Scale bar=500 μm.
701

702 **S3 Fig. Strain energy of myoblasts across substrate stiffnesses and ECM culture**
703 **conditions.** Bar graph showing strain energy of myoblasts cultured across substrate stiffness
704 and ECM conditions. n=19-24 cells per condition across N=3 biological replicates. Each data point
705 represents the mean of one biological replicate. Error bars report mean ± SD. Statistical
706 comparisons were made by two-way ANOVA followed by a Holm-Šídák multiple comparison test.
707

708 **S4 Fig. Strain energy of myoblasts with taut vs. wrinkled nuclei.** Bar graph showing strain
709 energy of myoblasts having taut (wrinkle index ≤ 20) vs. wrinkled (wrinkle index > 20) nuclei. n=16
710 cells in total across 2 technical replicates. Each data point represents one cell. Error bars report
711 mean ± SD. Statistical comparisons were made by a Student's t-test.
712

713 **S5 Fig. Proteomic profiling of myoblasts cultured on fibronectin-tethered soft (1 kPa) and**
714 **stiff (17 kPa) substrates A** Intensity heat map of all protein groups detected in myoblasts cultured
715 on soft and stiff substrate after filtering by the following criteria: at least 2 of the 3 technical
716 replicate runs have quantitative information; and more than 2100 proteins were quantified **B**

717 Volcano plot showing relative distributions of upregulated proteins in terms of -Log P-value and
718 expression difference (soft-stiff) of all detected proteins. Proteomic analysis was done on one cell-
719 line with 100,000 cells in each stiffness condition, and split into 3 technical replicates.
720
721 **S6 Fig. Expression of metabolic pathway components on soft (1 kPa) and stiff (17 kPa)**
722 **substrate. A** Heat map showing protein levels of metabolic enzymes involved in glycolysis and
723 pentose phosphate pathway in soft and stiff substrates **B** Heat map showing protein levels of ATP
724 synthase subunits on soft and stiff substrates.
725
726 **S7 Fig. Pax7/MyoD analysis of myoblasts cultured on fibronectin-tethered soft (1 kPa) and**
727 **stiff (17 kPa) substrate A** Representative confocal images of myogenic transcription factor
728 immunostaining. Hoechst-grey, Pax7-cyan, MyoD-yellow. Scalebar=20um. **B** Bar graph showing
729 the percentage of cells in each fate category (Pax7-/MyoD+, Pax7+/MyoD+, Pax7+/MyoD-, Pax7-
730 /MyoD-) on soft and stiff substrate. n=435-469 cells across N=3 biological replicates.
731
732

References

1. Li EW, McKee-Muir OC, Gilbert PM. Chapter Five - Cellular Biomechanics in Skeletal Muscle Regeneration. In: Sassoon D, editor. Current Topics in Developmental Biology. Academic Press; 2018. pp. 125–176. doi:10.1016/bs.ctdb.2017.08.007

2. Loreti M, Sacco A. The jam session between muscle stem cells and the extracellular matrix in the tissue microenvironment. Npj Regen Med. 2022;7: 1–15. doi:10.1038/s41536-022-00204-z

3. Silver JS, Günay KA, Cutler AA, Vogler TO, Brown TE, Pawlikowski BT, et al. Injury-mediated stiffening persistently activates muscle stem cells through YAP and TAZ mechanotransduction. Sci Adv. 2021;7: eabe4501. doi:10.1126/sciadv.abe4501

4. Lacraz G, Rouleau AJ, Couture V, Söllrald T, Drouin G, Veillette N, et al. Increased stiffness in aged skeletal muscle impairs muscle progenitor cell proliferative activity. PLoS ONE. 2015;10: 1–13. doi:10.1371/journal.pone.0136217

5. Trensz F, Lucien F, Couture V, Söllrald T, Drouin G, Rouleau AJ, et al. Increased microenvironment stiffness in damaged myofibers promotes myogenic progenitor cell proliferation. Skelet Muscle. 2015;5: 1–16. doi:10.1186/s13395-015-0030-1

6. Stearns-Reider KM, D'Amore A, Beezhold K, Rothrauff B, Cavalli L, Wagner WR, et al. Aging of the skeletal muscle extracellular matrix drives a stem cell fibrogenic conversion. Aging Cell. 2017;16: 518–528. doi:10.1111/acel.12578

7. Blanpied P, Smidt GL. The Difference in Stiffness of the Active Plantarflexors Between Young and Elderly Human Females. J Gerontol. 1993;48: M58–M63. doi:10.1093/geronj/48.2.M58

8. Wood LK, Kayupov E, Gumucio JP, Mendias CL, Claflin DR, Brooks SV. Intrinsic stiffness of extracellular matrix increases with age in skeletal muscles of mice. J Appl Physiol. 2014;117: 363–369. doi:10.1152/japplphysiol.00256.2014

9. Alnaqeeb MA, Al Zaid NS, Goldspink G. Connective tissue changes and physical properties of developing and ageing skeletal muscle. J Anat. 1984;139: 677–689.

10. Measuring changes in muscle stiffness after eccentric exercise using elastography - Green - 2012 - NMR in Biomedicine - Wiley Online Library. [cited 6 Feb 2023]. Available: https://analyticalsciencejournals.onlinelibrary.wiley.com/doi/full/10.1002/nbm.1801?casa_token=d2zuGJ30wkEAAAAA%3A7APVAtrFf9qMwz_o4a4cXzzH9ltS_OLw4Jf6pHIQJaVdK6dVPRmDK16OOzVHdKbOJkbQl5cQWFUpNQ

11. Lacourpaille L, Gross R, Hug F, Guével A, Péréon Y, Magot A, et al. Effects of Duchenne muscular dystrophy on muscle stiffness and response to electrically-induced muscle contraction: A 12-month follow-up. Neuromuscul Disord. 2017;27: 214–220. doi:10.1016/j.nmd.2017.01.001

12. Lacourpaille L, Hug F, Guével A, Péréon Y, Magot A, Hogrel J-Y, et al. Non-invasive assessment of muscle stiffness in patients with duchenne muscular dystrophy. Muscle Nerve. 2015;51: 284–286. doi:10.1002/mus.24445

13. Engler AJ, Griffin MA, Sen S, Bönnemann CG, Sweeney HL, Discher DE. Myotubes differentiate optimally on substrates with tissue-like stiffness: Pathological implications for soft or stiff microenvironments. J Cell Biol. 2004. doi:10.1083/jcb.200405004

14. Stedman HH, Sweeney HL, Shrager JB, Maguire HC, Panettieri RA, Petrof B, et al. The mdx mouse diaphragm reproduces the degenerative changes of Duchenne muscular dystrophy. Nature. 1991;352: 536–539. doi:10.1038/352536a0

15. Monge C, Distasio N, Rossi T, Sébastien M, Sakai H, Kalman B, et al. Quiescence of human muscle stem cells is favored by culture on natural biopolymeric films. 2017; 1–13. doi:10.1186/s13287-017-0556-8

16. Boontheekul T, Hill EE, Kong HJ, Mooney DJ. Regulating myoblast phenotype through controlled gel stiffness and degradation. Tissue Eng. 2007;13: 1431–1442. doi:10.1089/ten.2006.0356

17. Madl CM, Flaig IA, Holbrook CA, Wang YX, Blau HM. Biophysical matrix cues from the regenerating niche direct muscle stem cell fate in engineered microenvironments. Biomaterials. 2021;275: 120973. doi:10.1016/j.biomaterials.2021.120973

18. Bauer A, Gu L, Kwee B, Li WA, Dellacherie M, Celiz AD, et al. Hydrogel substrate stress-relaxation regulates the spreading and proliferation of mouse myoblasts. Acta Biomater. 2017. doi:10.1016/j.actbio.2017.08.041

19. Bunney PE, Zink AN, Holm AA, Billington CJ, Kotz CM. Hydrogel substrate stress-relaxation regulates the spreading and proliferation of mouse myoblasts. Physiol Behav. 2017;176: 139–148. doi:10.1016/j.physbeh.2017.03.040

20. Gilbert PM, Havenstrite KL, Magnusson KEG, Sacco A, Leonardi NA, Kraft P, et al. Substrate elasticity regulates skeletal muscle stem cell self-renewal in culture. Science. 2010;329: 1078–1081. doi:10.1126/science.1191035

21. Moyle LA, Cheng RY, Liu H, Davoudi S, Ferreira SA, Nissar AA, et al. Three-dimensional niche stiffness synergizes with Wnt7a to modulate the extent of satellite cell symmetric self-renewal divisions.

22. Brzóska E, Bello V, Darribère T, Moraczewski J. Integrin α3 subunit participates in myoblast adhesion and fusion in vitro. Differentiation. 2006;74: 105–118. doi:10.1111/j.1432-0436.2005.00059.x

23. Wilschut KJ, van Tol HTA, Arkesteijn GJA, Haagsman HP, Roelen BAJ. Alpha 6 integrin is important for myogenic stem cell differentiation. Stem Cell Res. 2011;7: 112–123. doi:10.1016/j.scr.2011.05.001

24. Rayagiri SS, Ranaldi D, Raven A, Mohamad Azhar NIF, Lefebvre O, Zammit PS, et al. Basal lamina remodeling at the skeletal muscle stem cell niche mediates stem cell self-renewal. Nat Commun. 2018;9: 1–12. doi:10.1038/s41467-018-03425-3

25. Gullberg D, Velling T, Lohikangas L, Tiger C-F. Integrins During Muscle Development and in Muscular Dystrophies. Pediatr Pathol Mol Med. 1998;18: 303–327. doi:10.1080/15513819809168793

811 26. Seetharaman S, Etienne-Manneville S. Integrin diversity brings specificity in
812 mechanotransduction. Biol Cell. 2018;110: 49–64. doi:10.1111/boc.201700060

813 27. Calve S, Simon H-G. Biochemical and mechanical environment cooperatively regulate
814 skeletal muscle regeneration. FASEB J. 2012;26: 2538. doi:10.1096/FJ.11-200162

815 28. Boonen KJM, Rosaria-Chak KY, Baaijens FPT, van der Schaft DWJ, Post MJ. Essential
816 environmental cues from the satellite cell niche: optimizing proliferation and differentiation.
817 Am J Physiol-Cell Physiol. 2009;296: C1338–C1345. doi:10.1152/ajpcell.00015.2009

818 29. Tse JR, Engler AJ. Preparation of Hydrogel Substrates with Tunable Mechanical
819 Properties. Curr Protoc Cell Biol. 2010;47: 10.16.1-10.16.16.
820 doi:10.1002/0471143030.cb1016s47

821 30. Afshar ME, Abraha HY, Bakooshli MA, Davoudi S, Thavandiran N, Tung K, et al. A 96-well
822 culture platform enables longitudinal analyses of engineered human skeletal muscle
823 microtissue strength. Sci Rep. 2020;10: 6918. doi:10.1038/s41598-020-62837-8

824 31. Afshar Bakooshli M, Lippmann ES, Mulcahy B, Iyer N, Nguyen CT, Tung K, et al. A 3D
825 culture model of innervated human skeletal muscle enables studies of the adult
826 neuromuscular junction. Brack A, Bronner ME, Brack A, editors. eLife. 2019;8: e44530.
827 doi:10.7554/eLife.44530

828 32. Pelham RJ, Wang Y. Cell locomotion and focal adhesions are regulated by
829 substrate flexibility. Proc Natl Acad Sci. 1997;94: 13661–13665.
830 doi:10.1073/pnas.94.25.13661

831 33. Martiel JL, Leal A, Kurzawa L, Balland M, Wang I, Vignaud T, et al. Measurement of cell
832 traction forces with ImageJ. Methods Cell Biol. 2015;125: 269–287.
833 doi:10.1016/bs.mcb.2014.10.008

834 34. Tseng Q, Duchemin-Pelletier E, Deshiere A, Balland M, Guillou H, Filhol O, et al. Spatial
835 organization of the extracellular matrix regulates cell–cell junction positioning. Proc Natl
836 Acad Sci. 2012;109: 1506–1511. doi:10.1073/pnas.1106377109

837 35. Cosgrove BD, Loebel C, Driscoll TP, Tsinman TK, Dai EN, Heo SJ, et al. Nuclear envelope
838 wrinkling predicts mesenchymal progenitor cell mechano-response in 2D and 3D
839 microenvironments. Biomaterials. 2021;270: 120662.
840 doi:10.1016/J.BIOMATERIALS.2021.120662

841 36. Iggo R. Lentiviral Transduction of Mammary Epithelial Cells. In: Vivanco M dM., editor.
842 Mammary Stem Cells: Methods and Protocols. New York, NY: Springer US; 2022. pp.
843 159–183. doi:10.1007/978-1-0716-2193-6_8

844 37. Schormann W, Hariharan S, Andrews DW. A reference library for assigning protein
845 subcellular localizations by image-based machine learning. J Cell Biol. 2020;219:
846 e201904090. doi:10.1083/jcb.201904090

847 38. Horzum U, Ozdil B, Pesen-Okvur D. Step-by-step quantitative analysis of focal adhesions.
848 MethodsX. 2014;1: 56–59. doi:10.1016/j.mex.2014.06.004

849 39. Urciuolo A, Quarta M, Morbidoni V, Gattazzo F, Molon S, Grumati P, et al. Collagen VI
850 regulates satellite cell self-renewal and muscle regeneration. Nat Commun. 2013;4: 1964.
851 doi:10.1038/ncomms2964

852 40. Safaee H, Bakooshli MA, Davoudi S, Cheng RY, Martowirogo AJ, Li EW, et al. Tethered
853 Jagged-1 Synergizes with Culture Substrate Stiffness to Modulate Notch-Induced
854 Myogenic Progenitor Differentiation. Cell Mol Bioeng. 2017;10: 501–513.
855 doi:10.1007/s12195-017-0506-7

856 41. Geiger B, Spatz JP, Bershadsky AD. Environmental sensing through focal adhesions. Nat
857 Rev Mol Cell Biol. 2009;10: 21–33. doi:10.1038/nrm2593

858 42. Wu C, Asokan SB, Berginski ME, Haynes EM, Sharpless NE, Griffith JD, et al. Arp2/3 Is
859 Critical for Lamellipodia and Response to Extracellular Matrix Cues but Is Dispensable for
860 Chemotaxis. Cell. 2012;148: 973–987. doi:10.1016/j.cell.2011.12.034

861 43. The small GTPase RhoG regulates microtubule-mediated focal adhesion disassembly |
862 Scientific Reports. [cited 7 Feb 2023]. Available: https://www.nature.com/articles/s41598-
863 019-41558-7

864 44. Bruno S, Crissman HA, Bauer KD, Darzynkiewicz Z. Changes in cell nuclei during S
865 Phase: Progressive chromatin condensation and altered expression of the proliferation-
866 associated nuclear proteins Ki-67, cyclin (PCNA), p105, and p34. Exp Cell Res. 1991;196:
867 99–106. doi:10.1016/0014-4827(91)90460-C

868 45. Gomes ER, Jani S, Gundersen GG. Nuclear Movement Regulated by Cdc42, MRCK,
869 Myosin, and Actin Flow Establishes MTOC Polarization in Migrating Cells. Cell. 2005;121:
870 451–463. doi:10.1016/j.cell.2005.02.022

871 46. Swaminathan V, Kalappurakkal JM, Mehta SB, Nordenfelt P, Moore TI, Koga N, et al. Actin
872 retrograde flow actively aligns and orients ligand-engaged integrins in focal adhesions.
873 Proc Natl Acad Sci. 2017;114: 10648–10653. doi:10.1073/pnas.1701136114

874 47. Vogel V, Sheetz M. Local force and geometry sensing regulate cell functions. Nat Rev Mol
875 Cell Biol. 2006;7: 265–275. doi:10.1038/nrm1890

876 48. Tilghman RW, Blais EM, Cowan CR, Sherman NE, Grigera PR, Jeffery ED, et al. Matrix
877 rigidity regulates cancer cell growth by modulating cellular metabolism and protein
878 synthesis. PloS One. 2012;7: e37231. doi:10.1371/journal.pone.0037231

879 49. Li L, Chambard JC, Karin M, Olson EN. Fos and Jun repress transcriptional activation by
880 myogenin and MyoD: the amino terminus of Jun can mediate repression. Genes Dev.
881 1992;6: 676–689. doi:10.1101/gad.6.4.676

882 50. Seong J, Tajik A, Sun J, Guan J-L, Humphries MJ, Craig SE, et al. Distinct biophysical
883 mechanisms of focal adhesion kinase mechanoactivation by different extracellular matrix
884 proteins. Proc Natl Acad Sci U S A. 2013;110: 19372–19377.
885 doi:10.1073/pnas.1307405110

51. Trappmann B, Gautrot JE, Connelly JT, Strange DGT, Li Y, Oyen ML, et al. Extracellular-matrix tethering regulates stem-cell fate. Nat Mater 2012 117. 2012;11: 642–649. doi:10.1038/nmat3339

52. Wen JH, Vincent LG, Fuhrmann A, Choi YS, Hribar K, Taylor-Weiner H, et al. Interplay of Matrix Stiffness and Protein Tethering in Stem Cell Differentiation. Nat Mater. 2014;13: 979. doi:10.1038/nmat4051

53. Baghdadi MB, Castel D, Machado L, Fukada S, Birk DE, Relaix F, et al. Reciprocal signalling by Notch–Collagen V–CALCR retains muscle stem cells in their niche. Nature. 2018;557: 714–718. doi:10.1038/s41586-018-0144-9

54. Zhang L, Noguchi Y, Nakayama H, Kaji T, Tsujikawa K, Ikemoto-Uezumi M, et al. The CalcR-PKA-Yap1 Axis Is Critical for Maintaining Quiescence in Muscle Stem Cells. Cell Rep. 2019;29: 2154-2163.e5. doi:10.1016/j.celrep.2019.10.057

55. Vachon PH, Xu H, Liu L, Loechel F, Hayashi Y, Arahata K, et al. Integrins (␣7␤1) in Muscle Function and Survival.

56. Rozo M, Li L, Fan CM. Targeting β1-integrin signaling enhances regeneration in aged and dystrophic muscle in mice. Nat Med. 2016;22: 889–896. doi:10.1038/nm.4116

57. Gu J, Sumida Y, Sanzen N, Sekiguchi K. Laminin-10/11 and Fibronectin Differentially Regulate Integrin- dependent Rho and Rac Activation via p130Cas-CrkII-DOCK180 Pathway *. J Biol Chem. 2001;276: 27090–27097. doi:10.1074/jbc.M102284200

58. Goodman SL, Risse G, von der Mark K. The E8 subfragment of laminin promotes locomotion of myoblasts over extracellular matrix. J Cell Biol. 1989;109: 799–809. doi:10.1083/jcb.109.2.799

59. Kann AP, Hung M, Wang W, Nguyen J, Gilbert PM, Wu Z, et al. An injury-responsive Rac-to-Rho GTPase switch drives activation of muscle stem cells through rapid cytoskeletal remodeling. Cell Stem Cell. 2022;29: 933-947.e6. doi:10.1016/j.stem.2022.04.016

60. Tierney MT, Sacco A. Satellite Cell Heterogeneity in Skeletal Muscle Homeostasis. Trends Cell Biol. 2016;26: 434–444. doi:10.1016/J.TCB.2016.02.004

61. Buxboim A, Irianto J, Swift J, Athirasala A, Shin JW, Rehfeldt F, et al. Coordinated increase of nuclear tension and lamin-A with matrix stiffness outcompetes lamin-B receptor that favors soft tissue phenotypes. Mol Biol Cell. 2017;28: 3333–3348. doi:10.1091/MBC.E17-06-0393/ASSET/IMAGES/LARGE/3333FIG8.TIF.GZ.JPEG

62. Kim J-K, Louhghalam A, Lee G, Schafer BW, Wirtz D, Kim D-H. Nuclear lamin A/C harnesses the perinuclear apical actin cables to protect nuclear morphology. Nat Commun. 2017;8: 2123. doi:10.1038/s41467-017-02217-5

63. Dantas M, Oliveira A, Aguiar P, Maiato H, Ferreira JG. Nuclear tension controls mitotic entry by regulating cyclin B1 nuclear translocation. J Cell Biol. 2022;221: e202205051. doi:10.1083/jcb.202205051

923 64. Mills GB, Moolenaar WH. The emerging role of lysophosphatidic acid in cancer. Nat Rev
924 Cancer. 2003;3: 582–591. doi:10.1038/nrc1143

925 65. Manning Jr. TJ, Rosenfeld SS, Sontheimer H. Lysophosphatidic acid stimulates
926 actomyosin contraction in astrocytes. J Neurosci Res. 1998;53: 343–352.
927 doi:10.1002/(SICI)1097-4547(19980801)53:3<343::AID-JNR8>3.0.CO;2-A

928 66. Lin M-E, Herr DR, Chun J. Lysophosphatidic acid (LPA) receptors: signaling properties and
929 disease relevance. Prostaglandins Other Lipid Mediat. 2010;91: 130–138.
930 doi:10.1016/j.prostaglandins.2009.02.002

931 67. Elosegui-Artola A, Andreu I, Beedle AEM, Lezamiz A, Uroz M, Kosmalska AJ, et al. Force
932 Triggers YAP Nuclear Entry by Regulating Transport across Nuclear Pores. Cell.
933 2017;171: 1397-1410.e14. doi:10.1016/J.CELL.2017.10.008

934 68. Andreu I, Granero-Moya I, Chahare NR, Clein K, Molina-Jordán M, Beedle AEM, et al.
935 Mechanical force application to the nucleus regulates nucleocytoplasmic transport. Nat
936 Cell Biol. 2022;24: 896–905. doi:10.1038/s41556-022-00927-7

937 69. Jacchetti E, Nasehi R, Boeri L, Parodi V, Negro A, Albani D, et al. The nuclear import of
938 the transcription factor MyoD is reduced in mesenchymal stem cells grown in a 3D micro-
939 engineered niche. Sci Rep 2021 111. 2021;11: 1–19. doi:10.1038/s41598-021-81920-2

940

Fig 1.

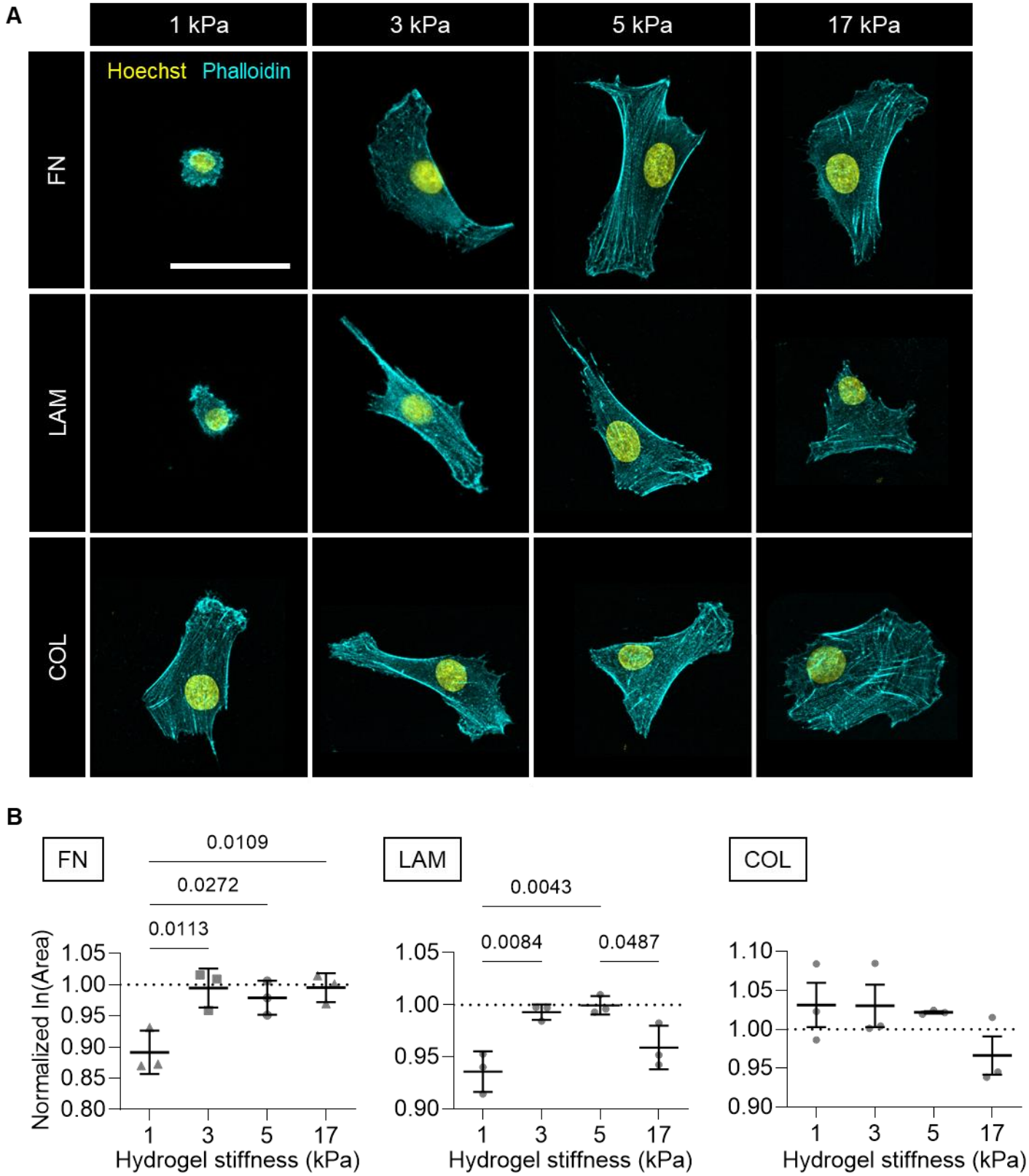
A
1 kPa
3 kPa
5 kPa
17 kPa
Hoechst
Phalloidin
FN
LAM
COL
B
FN
0.0109
0.0272
0.0113
Normalized ln(Area)
1.05
1.00
0.95
0.90
0.85
0.80
1
3
5
17
Hydrogel stiffness (kPa)
LAM
0.0043
0.0084
0.0487
1.05
1.00
0.95
0.90
1
3
5
17
Hydrogel stiffness (kPa)
COL
1.10
1.05
1.00
0.95
0.90
1
3
5
17
Hydrogel stiffness (kPa)

Fig 2.

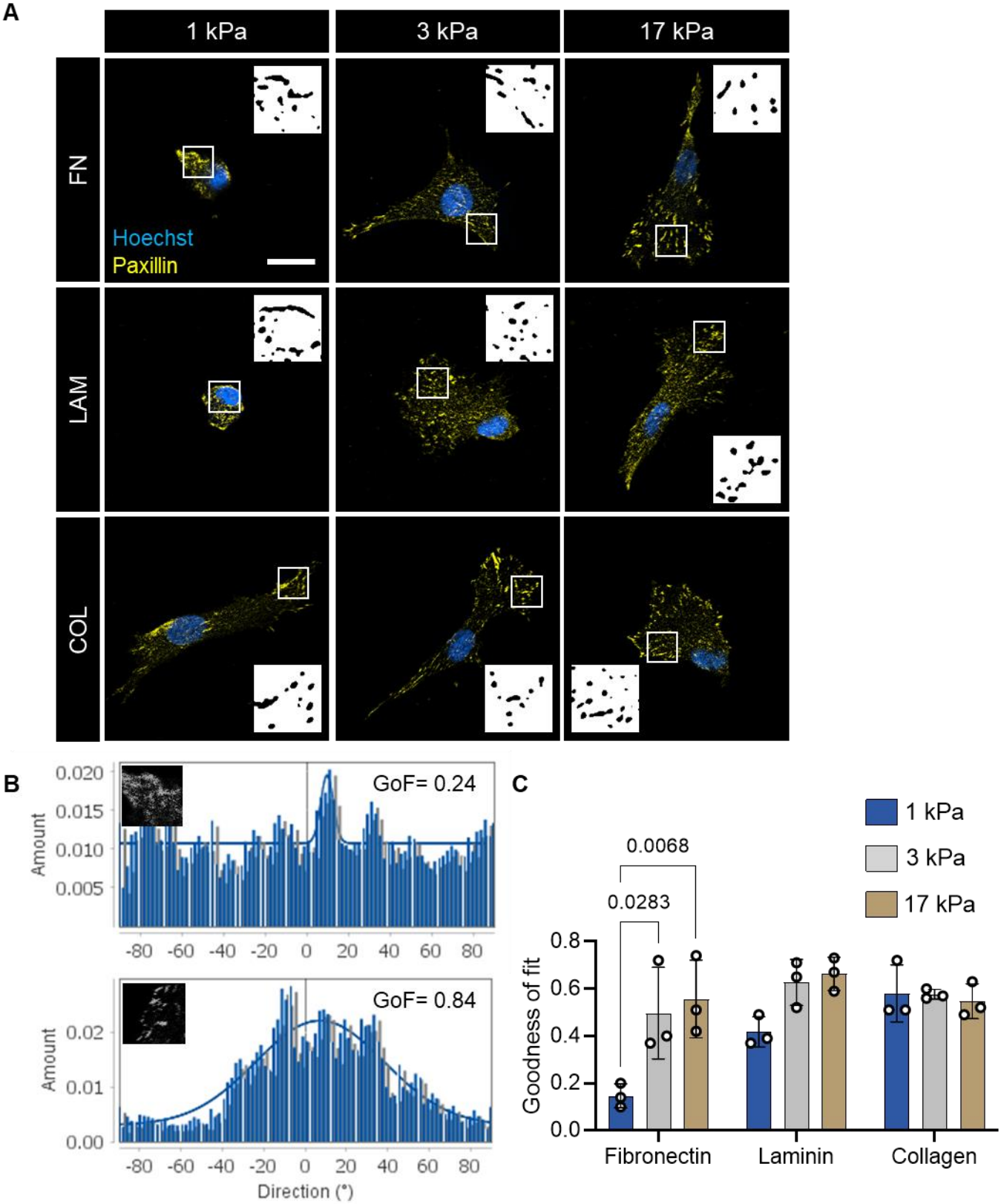
A
1 kPa
3 kPa
17 kPa
FN
LAM
COL
Hoechst
Paxillin
B
GoF= 0.24
GoF= 0.84
Amount
Direction (°)
C
1 kPa
3 kPa
17 kPa
0.0068
0.0283
Goodness of fit
Fibronectin
Laminin
Collagen

Fig 3.

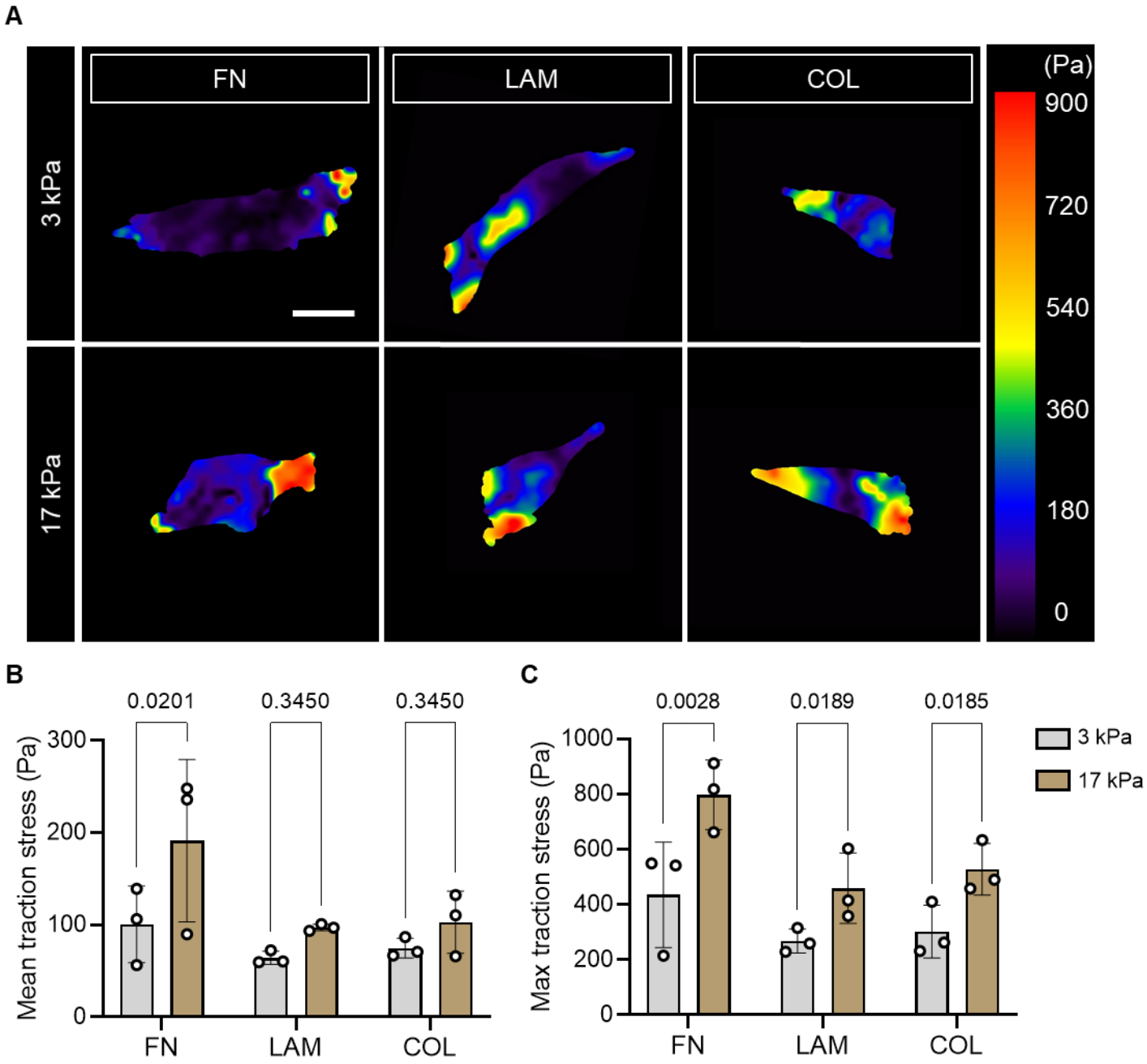
A
FN
LAM
COL
3 kPa
17 kPa
(Pa)
900
720
540
360
180
0
B
0.0201
0.3450
0.3450
Mean traction stress (Pa)
300
200
100
0
FN
LAM
COL
C
0.0028
0.0189
0.0185
Max traction stress (Pa)
1000
800
600
400
200
0
FN
LAM
COL
3 kPa
17 kPa

Fig 4.

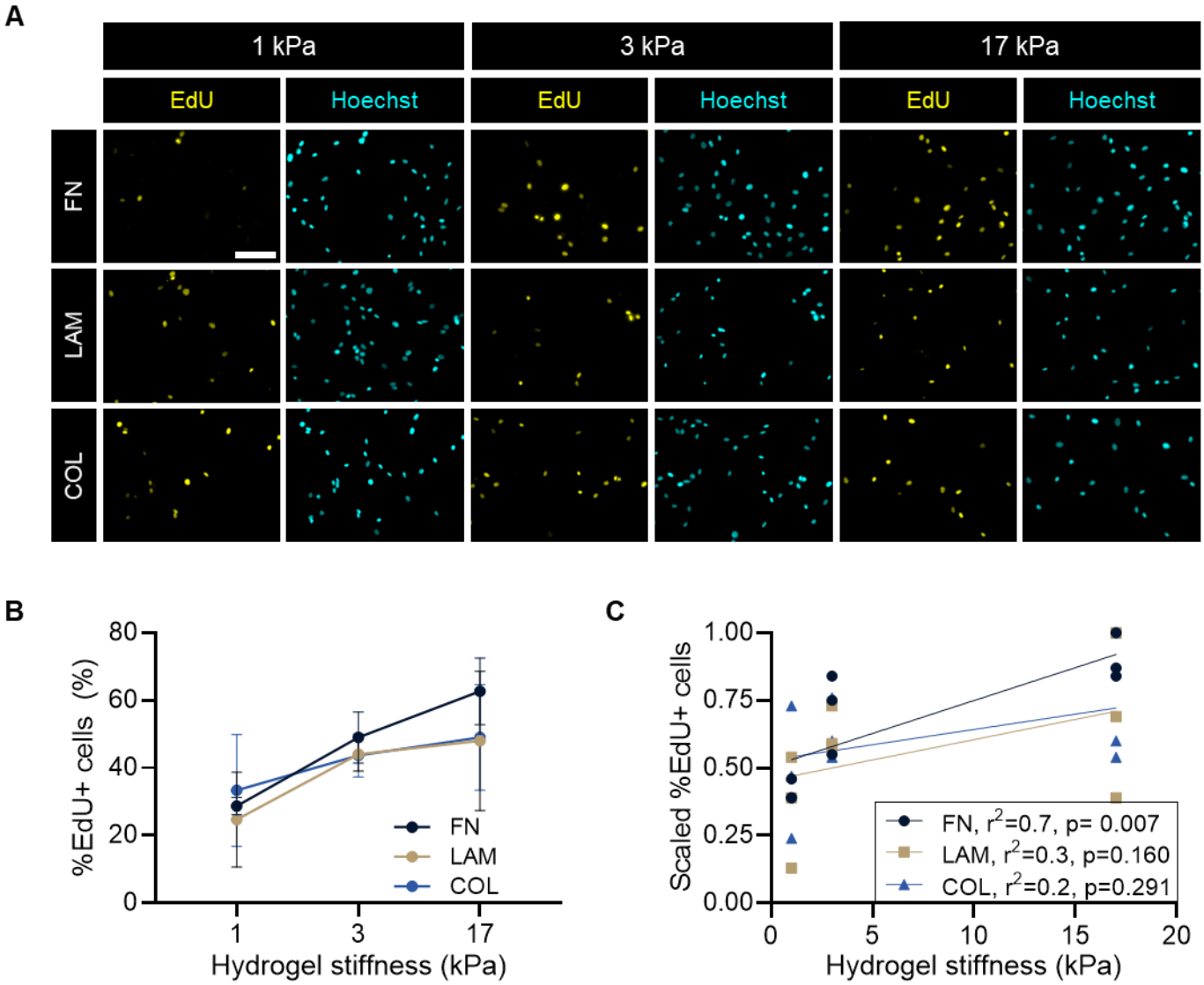
A
1 kPa
3 kPa
17 kPa
EdU
Hoechst
FN
LAM
COL
B
%EdU+ cells (%)
Hydrogel stiffness (kPa)
FN
LAM
COL
C
Scaled %EdU+ cells
Hydrogel stiffness (kPa)
FN, r2=0.7, p= 0.007
LAM, r2=0.3, p=0.160
COL, r2=0.2, p=0.291

Fig 5.

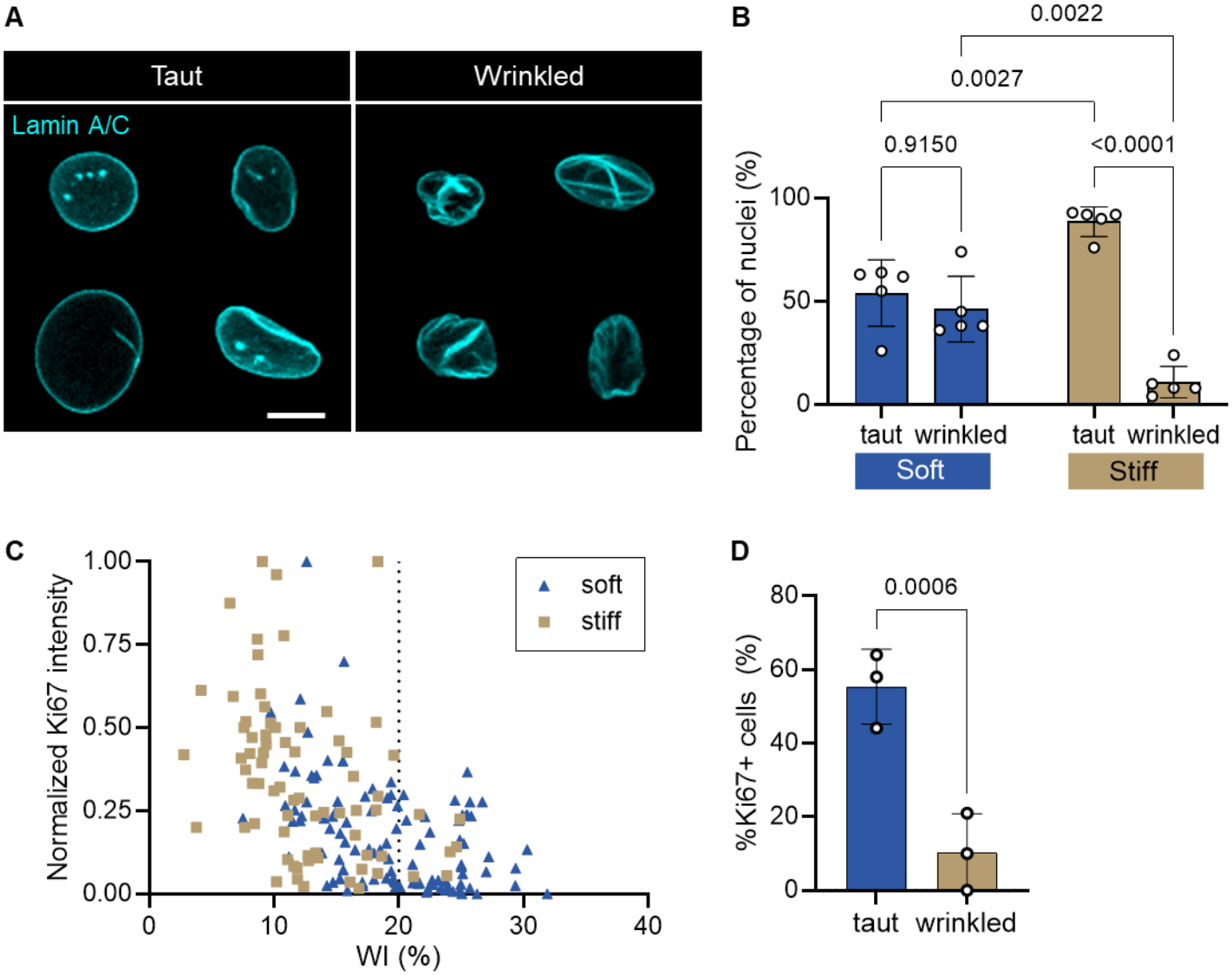
A
Taut
Wrinkled
Lamin A/C
B
0.0022
0.0027
0.9150
<0.0001
Percentage of nuclei (%)
100
50
0
taut
wrinkled
taut
wrinkled
Soft
Stiff
C
Normalized Ki67 intensity
1.00
0.75
0.50
0.25
0.00
0
10
20
30
40
WI (%)
soft
stiff
D
%Ki67+ cells (%)
80
60
40
20
0
0.0006
taut
wrinkled

Fig 6.

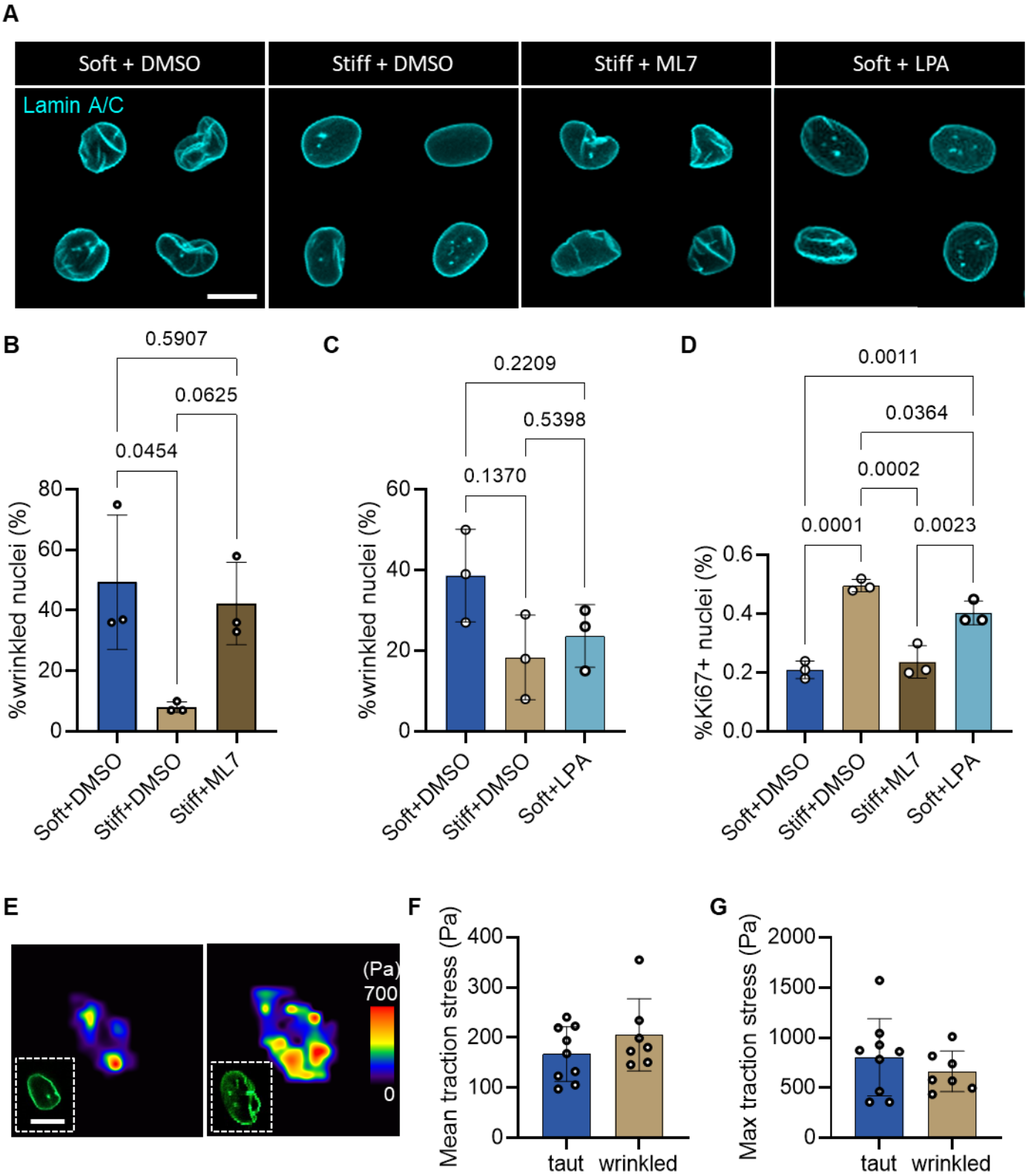
A
Soft + DMSO
Stiff + DMSO
Stiff + ML7
Soft + LPA
Lamin A/C
B
0.5907
0.0625
0.0454
%wrinkled nuclei (%)
80
60
40
20
0
Soft+DMSO
Stiff+DMSO
Stiff+ML7
C
0.2209
0.5398
0.1370
%wrinkled nuclei (%)
60
40
20
0
Soft+DMSO
Stiff+DMSO
Soft+LPA
D
0.0011
0.0364
0.0002
0.0001
0.0023
%Ki67+ nuclei (%)
0.6
0.4
0.2
0.0
Soft+DMSO
Stiff+DMSO
Stiff+ML7
Soft+LPA
E
(Pa)
700
0
F
Mean traction stress (Pa)
400
300
200
100
0
taut
wrinkled
G
Max traction stress (Pa)
2000
1500
1000
500
0
taut
wrinkled

Fig 7.

A

PANTHER pathways	# genes	Fold enrichment	Raw P-value
Pentose phosphate pathway	4	11.28	1.11E-03
Glycolysis	8	10.15	6.51E-06
Integrin signaling pathway	27	3.43	1.55E-07
Cytoskeletal regulation by Rho GTPase	11	3.25	1.11E-03
Huntington disease	15	2.51	1.76E-03
Unclassified	666	0.94	3.74E-05

B

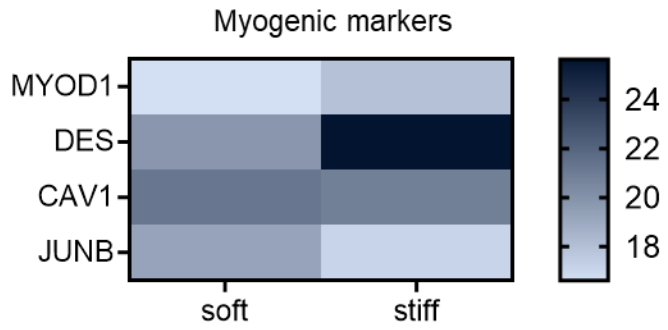

C

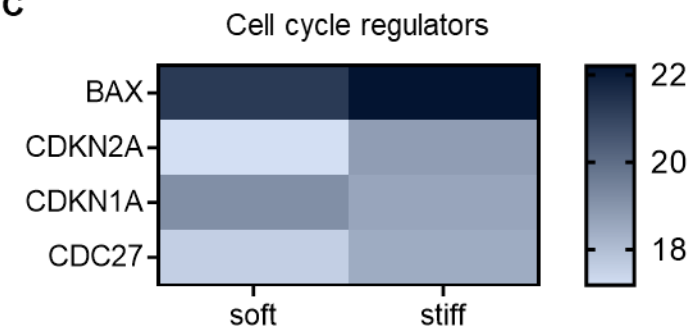

D

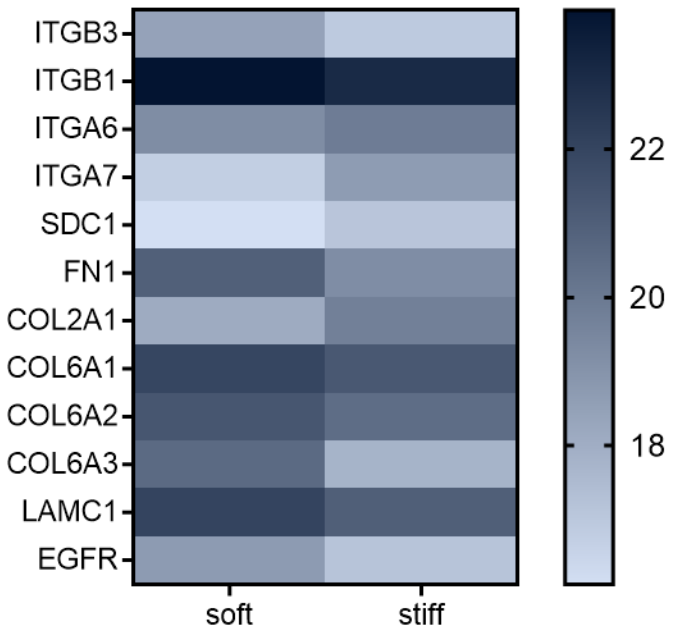

E

GO cellular component enrichment

Upregulated in soft condition	Upregulated in stiff condition
Ribonucleoprotein complex	Nucleus
Membrane-enclosed lumen	Nucleoplasm
Intracellular organelle lumen	Nuclear lumen
Nucleolus	Ribonucleoprotein complex
Organelle lumen	Intracellular organelle